

Point defect formation at finite temperatures with machine learning force fields

Irea Mosquera-Lois,¹ Johan Klarbring,^{1,2} and Aron Walsh^{1, a)}

¹*Thomas Young Centre & Department of Materials, Imperial College London, London SW7 2AZ, UK*

²*Department of Physics, Chemistry and Biology (IFM), Linköping University, SE-581 83, Linköping, Sweden*

(Dated: 24 December 2024)

Point defects dictate the properties of many functional materials. The standard approach to modelling the thermodynamics of defects relies on a static description, where the change in Gibbs free energy is approximated by the internal energy. This approach has a low computational cost, but ignores contributions from atomic vibrations and structural configurations that can be accessed at finite temperatures. We train a machine learning force field (MLFF) to explore dynamic defect behaviour using Te_i^{+1} and V_{Te}^{+2} in CdTe as exemplars. We consider the different entropic contributions (e.g., electronic, spin, vibrational, orientational, and configurational) and compare methods to compute the defect free energies, ranging from a harmonic treatment to a fully anharmonic approach based on thermodynamic integration. We find that metastable configurations are populated at room temperature and thermal effects increase the predicted concentration of Te_i^{+1} by two orders of magnitude — and can thus significantly affect the predicted properties. Overall, our study underscores the importance of finite-temperature effects and the potential of MLFFs to model defect dynamics at both synthesis and device operating temperatures.

^{a)}Electronic mail: a.walsh@imperial.ac.uk

I. INTRODUCTION

Point defects make or break material functionality¹. They limit photovoltaic efficiency by acting as non-radiative recombination centres, control ionic conductivity in batteries, provide active sites for catalytic reactions, and platforms for quantum information technologies. Despite their profound effect on the macroscopic properties of crystals, they are present in dilute concentrations and thus render experimental characterisation challenging. As a result, a combination of experiment and theory is needed to understand defect behaviour.

The key factor when modelling defects is their concentration, which is determined by the free energy of defect formation, g_f , at the synthesis or annealing temperature. Calculating g_f is however computationally challenging, and is thus typically approximated by the formation internal energy, $u_f(0\text{ K})$, i.e. $g_f(T_{\text{synthesis}}) \approx u_f(0\text{ K})$ ^{2,3}. Inherent in this approximation is the assumption of a *static* framework, where most studies only consider the defect ground state structure at 0 K, and thus neglect metastable configurations that may be populated at the device operating temperature. Since the properties of a defect strongly depend on its geometry⁴⁻⁹, the predicted behaviour can be significantly affected when ignoring thermally accessible metastable configurations¹⁰⁻¹⁶.

With the development of better computational resources, more accurate studies that go beyond this static 0 K approximation are becoming possible using *ab-initio* methods. In the last decades, many investigations have modelled entropic contributions for defects in elementary solids¹⁷⁻⁶¹. Thermal effects are harder to model in multinary semiconductors due to the higher number of possible intrinsic charged defects and required level of theory, but have been included for specific defects⁶²⁻⁸⁰. However, most of these studies adopt several approximations: i) they only account for vibrational entropies, thereby neglecting other degrees of freedom (e.g., electronic, spin, orientational and configurational), and ii) they adopt the (quasi)harmonic approximation to model vibrational effects (e.g., assuming a quadratic potential energy surface for the interatomic bonds). The limitations of these approximations are system-dependent and not well investigated, and demonstrate the lack of

a reliable and affordable approach to model thermal effects for defects.

In this study, we target these limitations by considering all relevant entropic contributions and systematically comparing the different methods to calculate the defect formation free energy, ranging from a harmonic to a fully anharmonic approach based on thermodynamic integration (TI). To reduce the cost of these simulations, we use machine learning force fields as a surrogate model, which successfully map the defect energy surfaces (Section II A). We choose Te_i^{+1} and V_{Te}^{+2} in CdTe as exemplar systems since they display potential energy surfaces of different complexity (e.g., presence *versus* lack of low-energy metastable configurations¹²) (Section II B). By modelling the impact of thermal effects on their predicted defect concentrations, we find that these dominate when the defect undergoes symmetry-breaking structural reconstructions and has low-energy metastable configurations, thereby demonstrating the limitations of the idealised 0 K description (Section II C).

II. RESULTS

A. Machine learning force fields for defects

Calculating the defect formation free energy, g_f , requires modelling the defect formation reaction by computing the free energy difference between products and reactants at the synthesis temperature.^{2,3} For example, the formation of the positively charged tellurium interstitial, Te_i^{+1} , can be described by the defect reaction



The corresponding formation free energy is defined from the sum of products (charged defect with an electron in the conduction band) minus the sum of reactants (pristine CdTe host and reservoir of Te). In the standard first-principles supercell formalism, this formation energy is given by

$$g_f = g(\text{Cd}_n\text{Te}_{n+1}^{+1}) - g(\text{Te}) - g([\text{CdTe}]_n) + E_F + E_{corr} \quad (2)$$

where Te represents the phase that acts as the external source of atoms during synthesis, E_F denotes the Fermi level and E_{corr} is the correction energy for charged defects. From these terms, the defect free energy, $g(\text{Cd}_n\text{Te}_{n+1}^{+1})$, is the most challenging to compute due to the low symmetry and large supercells required to model defects (e.g., many force calculations in the (quasi)harmonic method). This is exacerbated when going beyond the harmonic approximation since computing the *anharmonic* free energy with TI requires many and long molecular dynamics runs.^{81,82}

To reduce the cost of free energy calculations, we employ machine learning force fields and train a separate MACE model⁸³ for each system involved in the defect formation reaction, targeting temperatures ranging from 100 K to the typical CdTe anneal temperature of 840 K⁸⁴. All models show good accuracies with low mean and root mean square errors on the test set (see TABLE I and further discussion in Methods and Supporting Information (SI)). The accuracy of the defect models is further confirmed by mapping the one-dimensional path between the stable defect structures, which shows good agreement despite the small energy difference between the distinct configurations of Te_i^{+1} (Fig. 1 and SI Supplementary Figure S9).

B. Defect dynamics at room temperature

We first investigate the limitations of the static framework by comparing the behaviour of the defects at 0 K and around the typical operating temperature for a solar cell (300 K). The potential energy surface calculated at 0 K shows that Te_i^{+1} is a bistable defect with two accessible structures: a split configuration with either one or two Te-Te bonds¹², which have C_{2v} and C_s site symmetries, respectively, and an energy difference of $\Delta E(C_s - C_{2v}) = 18$ meV (Fig. 1). In contrast, V_{Te}^{+2} only has one accessible structure at the device operating conditions since the metastable C_{3v} configuration is 1.8 eV above the T_d ground state ($\gg k_B T = 25$ meV at 300 K).

To validate these predictions, we perform molecular dynamics under the NPT ensemble

TABLE I Mean absolute errors and root mean square errors (shown in parentheses) of the test sets for energies, forces and stresses. The relatively high errors observed for Te are caused by including its liquid phase ($T_{\text{melt}} \approx 704$ K). Distributions of the absolute errors and the learning curve for the Te_i^{+1} model are shown in the Supporting Information.

System	Energy (meV/atom)	Force (meV/Å)	Stress (meV/Å ³)
CdTe	0.3 (0.4)	13 (17)	0.2 (0.3)
Te_i^{+1}	0.5 (0.7)	21 (30)	0.2 (0.3)
V_{Te}^{+2}	0.4 (0.6)	18 (24)	0.2 (0.3)
Te	1.6 (2.3)	73 (102)	0.9 (1.3)

(300 K, 1 atm, 1 ns), revealing three distinct motions for Te_i^{+1} (Fig. 2). The fastest process corresponds to changes in *configuration* between the C_{2v} and C_s geometries, which is reflected by variations in the distances between Te_i^{+1} and its neighbouring Te atoms as it alternates between forming 1 and 2 Te-Te bonds. On a slower timescale, there are changes in the defect *position* (i.e., hopping between lattice sites) as well as changes in the *orientation* of the Te-Te bond, indicated by variation in the angle between the Te-Te bond(s) and the lattice axes. These three motions occur rapidly on the nanosecond timescale due to their low energy barriers relative to the thermal energy ($E_b = 28 - 100$ meV) with rates on the order of 10^{10} s⁻¹ (configurational and hopping) and 10^8 s⁻¹ (rotation) — and highlight the configurational, orientational and migration degrees of freedom that contribute to the defect formation entropy. In contrast, this dynamic behaviour of Te_i^{+1} differs significantly from that of V_{Te}^{+2} , which remains stable in its T_d ground state configuration, as depicted in [Supplementary Figure S12](#), and is thus well-described by its static 0 K structure.

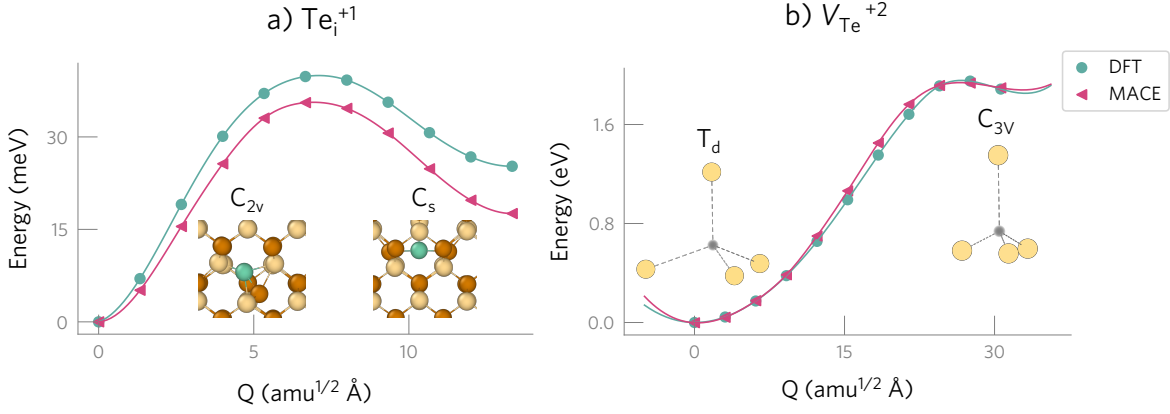


Fig. 1 Potential energy surfaces illustrating the defect configurations identified with defect structure searching⁸⁵, calculated with DFT (green circles) and MACE (pink triangles). a) Te_i^{+1} is a bistable defect since the metastable configuration (split Te-Cd with C_s symmetry) is only 18 meV higher than the ground state (split Te-Te with C_{2v} symmetry). Note that the differences between DFT and MACE are in meV/*supercell*, with the error in $\Delta E(C_{2v} - C_s)$ only accounting to 0.1 meV/*atom*. b) V_{Te}^{+2} , where the metastable configuration (C_{3v}) is significantly higher in energy (1.8 eV above the ground state structure of T_d symmetry). Te in brown, Cd in yellow, Te_i^{+1} in green and V_{Te}^{+2} in shaded grey.

C. Impact of defect entropy on predicted concentrations

The dynamic behaviour of Te_i^{+1} suggests that its formation entropy, s_f , will be significant at the CdTe annealing temperature (≈ 840 K)⁸⁴ and will thus affect the predicted equilibrium concentration. To verify this, we calculate s_f and g_f by considering the different degrees of freedom that change upon forming the defect at a fixed lattice site: electronic, spin, vibrational, orientational and structural (also referred to as configurational).² While the first three terms can be estimated with analytical expressions (see Methods), the vibrational contribution is more challenging and typically requires approximations. By assuming a quadratic energy surface for the interatomic bonds, the harmonic vibrational g_f can be calculated, which can be extended to account for thermal expansion with the quasiharmonic

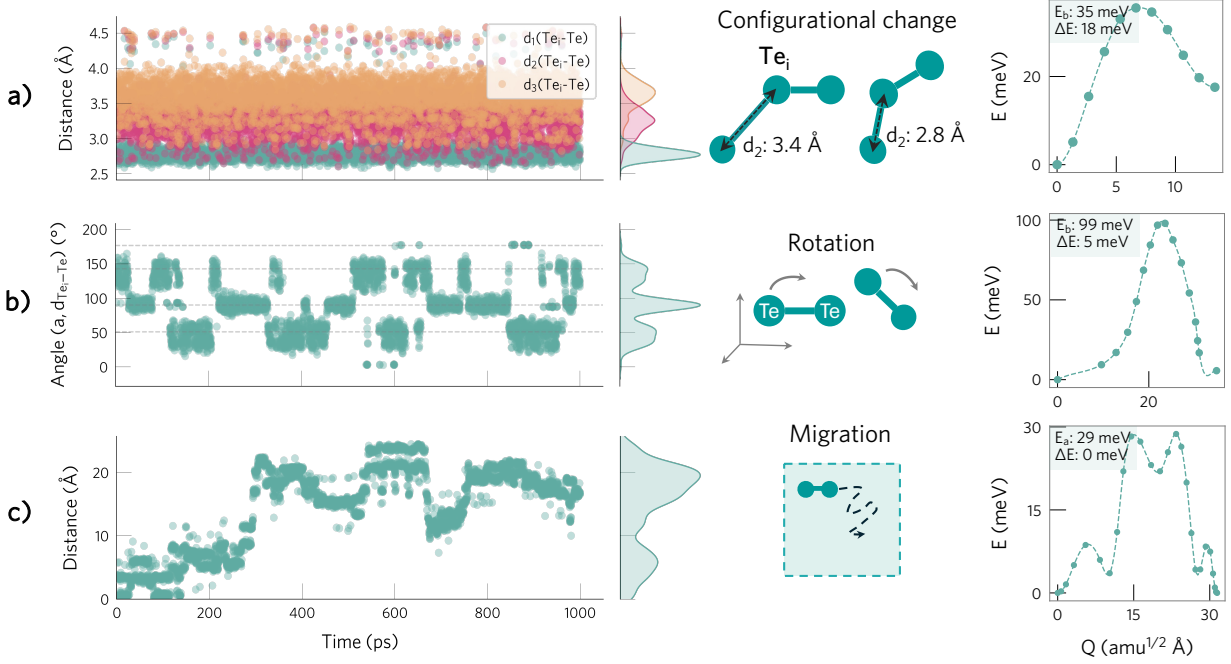


Fig. 2 Active degrees of freedom of Te_i^{+1} at 300 K and associated energy barriers. a) Configurational change, reflected by changes in the Te_i -Te distances. The narrow green peak illustrates the shortest Te_i -Te bond, which shows little variation at around 2.8 Å, while the wider pink and orange distributions demonstrate the wide variation in the second and third shortest Te-Te distances (see [Supplementary Figure S11](#)). b) Changes in the orientation of the Te_i -Te bond with respect to the [100] direction. c) Migration, illustrated by tracking the distance between the current and original position of the interstitial.

approximation^{2,86}. However, this harmonic assumption might be limited for defects at high temperatures, where anharmonic effects seem to be important – as suggested by the high anharmonicity scores⁸⁷ observed for Te_i^{+1} relative to pristine CdTe ($\sigma(840 \text{ K}) = 4.5$ versus 0.8, respectively, and σ typically ranging between 0 – 1; [Supplementary Figure S13](#)).

To assess these limitations, we use non-equilibrium thermodynamic integration to account for anharmonic effects and compare the g_f calculated with each approach. We do this by starting from the Einstein crystal (independent harmonic oscillators), integrating to the

anharmonic crystal at 100 K, and finally integrating with respect to temperature up to 840 K (see Methods for further details). Since TI calculates the change in the *total* free energy described by the MACE potential (i.e., the ionic degrees of freedom), it already includes the vibrational, orientational and structural contributions, and thus we only have to add the electronic and spin terms to $g_f^{anh}(T)$. We define three defect formation free energies with increasing accuracy:

$$\begin{aligned} g_f^{harm}(T) &= g_f^{vib,harm}(T) - T s_f^{orient} - T s_f^{struc}(T) - T s_f^{spin} - T s_f^{elec}(T) \\ g_f^{quasi}(T) &= g_f^{vib,quasi}(T) - T s_f^{orient} - T s_f^{struc}(T) - T s_f^{spin} - T s_f^{elec}(T) \\ g_f^{anh}(T) &= g_f^{TI}(T) - T s_f^{spin} - T s_f^{elec}(T). \end{aligned} \quad (3)$$

where the (quasi)harmonic vibrational free energy, $g_f^{vib,harm}$, refers to the ground state structure (further details in Methods). Here, the (quasi)harmonic approach decouples *all* the degrees of freedom, and thus assumes that the timescales for these processes are sufficiently different to avoid significant mixing², while the anharmonic formalism only decouples the electronic from the ionic motions.

We follow the standard convention in defect chemistry and define g_f as the change in free energy for forming a defect at a *fixed* lattice site (i.e., excluding entropic contributions from the mixing or site entropy^a). We calculate the equilibrium defect concentration with

$$[c] = \frac{N_{sites}}{V} \exp\left(\frac{-g_f}{k_B T}\right) \quad (4)$$

where V denotes the crystallographic unit cell volume and N_{sites} the number of symmetry-equivalent sites where the defect can form in the unit cell.

As demonstrated in Fig. 3.b, for Te_i^{+1} thermal effects are significant at annealing temperature, with $g_f(840 \text{ K})$ differing by 0.5 eV from $u_f(0 \text{ K}) - T(s_f^{spin} + s_f^{orient})$. All methods are in good agreement, indicating that the harmonic approximation gives a reasonable estimate

^a This mixing entropy arises from the different ways in which a defect can be arbitrarily placed in the symmetry-equivalent lattice sites and depends on the *equilibrium* defect concentration. Due to this dependence on c , it is separated from the free energy of forming the defect at a fixed site (g_f , which is independent of c within the dilute limit) when deriving the expression for the defect concentration.²

of g_f , since anharmonic effects approximately cancel out between the bulk and the defect. This agreement also validates the decoupling approximation used to separate the different degrees of freedom (e.g., $g_f^{TI} \approx g_f^{vib,harm} - T s_f^{orient} - T s_f^{struc}$). Using this approximation, we find that their relative entropic contributions follow the expected trend, with the vibrational one dominating, followed by the structural, spin, orientational and electronic terms (with $s_f(840 \text{ K})$ of 4.2, 0.7, 0.7, -0.7 and 0.1 k_B , respectively; Fig. 3.a). However, we note that the structural term can become larger for defects that have many low-energy metastable configurations.²⁵

Overall, the total entropic contribution is not negligible and significantly affects g_f , increasing the predicted concentration by a factor of 500 (Fig. 3.c). This importance of entropic effects contrasts with their role in $V_{\text{Te}^{+2}}$, where they are almost negligible ($g_f(840 \text{ K}) - u_f(0 \text{ K}) = 0.08 \text{ eV}$; Supplementary Figure S14) due to i) smaller magnitude of the vibrational entropy and ii) lack of spin, orientational and structural entropies. As a result, we expect thermal effects to be important for defects which i) introduce strong structural distortions (high s_f^{vib}), ii) break the host site symmetry (high s_f^{orient}), and iii) have low-energy metastable configurations (high s_f^{struc}).

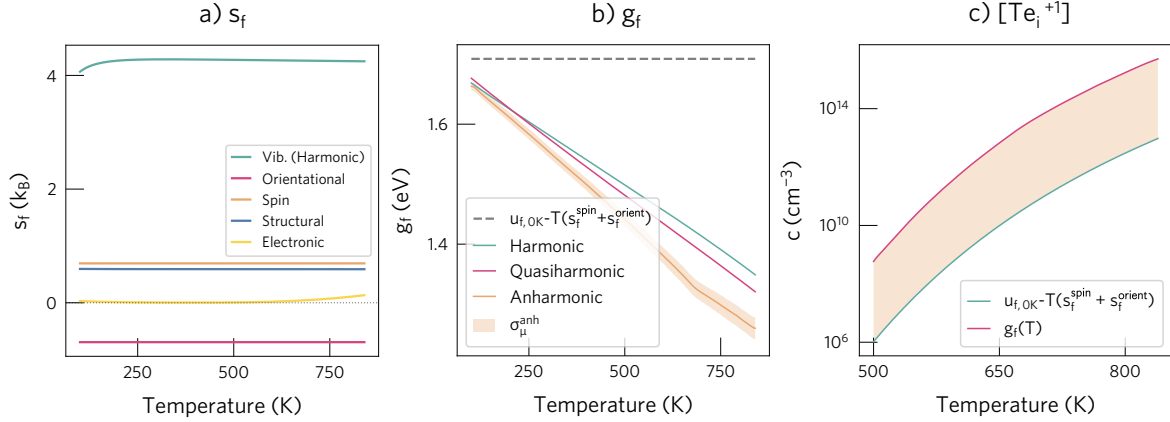


Fig. 3 a) Contribution of the different degrees of freedom to the formation entropy of Te_i^{+1} . Note that s_f^{orient} is negative since the symmetry increases when going from the initial to the relaxed interstitial structure (see Methods). b) Comparison of approximations for calculating the defect formation free energy of Te_i^{+1} , $g_f(T)$. The shaded orange area illustrates the estimated error in the thermodynamic integration simulations, defined as the standard error of the mean free energy, σ_{μ}^{anh} (details in Methods). For comparison, the formation internal energy with the spin and orientational entropies, $u_f(0 \text{ K}) - T(s_f^{spin} + s_f^{orient})$, typically used in most defect studies, is shown with a dashed grey line. c) Effect of including the entropic contribution for predicting the defect concentration.

III. DISCUSSION

Overall, we have illustrated how to model thermal effects for point defects in crystals, demonstrating the dynamic character of Te_i^{+1} in CdTe, which rapidly changes between configuration, orientation and position at room temperature. These degrees of freedom increase the entropy upon defect formation, and can be computed from standard defect calculations as illustrated in this study. The computationally challenging term is the vibrational entropy. We have found that the harmonic approximation gives a reasonable and affordable description of the vibrational formation entropy at 840 K for a dynamic defect with a high anharmonicity score. This suggests the validity of the harmonic approximation for ‘simpler’ defects with

single configurations that do not diffuse in this temperature regime.

By combining the different entropic contributions, we find that thermal effects increase the predicted concentration of Te_i^{+1} by two orders of magnitude, and can thus significantly affect the predicted behaviour by shifting the relative defect populations. Thermal effects will play a significant role for defects that undergo structural reconstructions, break the site symmetry of the host and have low-energy metastable configurations (high s_f^{vib} , s_f^{orient} and s_f^{struc}), as illustrated by comparing two defects with energy surfaces of different complexity. Beyond defect related factors, hosts with a soft and dynamic lattice or compositional disorder will also be more sensitive to thermal effects, since their defects typically lead to stronger reconstructions (e.g., rebonding or local octahedral rotations in perovskite structures⁸⁸) and display many low-energy metastable configurations (e.g., Sb_2Se_3 ⁸ or alloys⁸⁹ like $\text{CdSe}_x\text{Te}_{(1-x)}$ ⁹⁰). A special case is materials where the phase relevant for applications is only stable at finite temperatures. Here, it can be key to model defects at the device operating temperature since their behaviour can be very sensitive to its surrounding structure — as illustrated by the discrepancies when modelling the carrier capture behaviour of I_i in different phases of CsPbI_3 ⁹¹.

Despite the importance of including thermal effects for accurate defect predictions, the current limitation is the computational cost. While the orientational, spin and electronic terms can be calculated from standard defect calculations using the `doped` package⁹², the configurational term requires considering the different thermally-accessible structures of a defect, which can be identified through defect-structure searching methods like `ShakeNBreak`⁸⁵. More challenging is the vibrational term as it requires going beyond standard static defect calculations. In practice, accounting for this contribution will only be affordable for high-accuracy studies that target the low-energy defects; especially for applications with a high synthesis or operating temperature, like industrial thermoelectrics, thermochemical water splitting, exhaust automotive catalysts or solid-state fuel cells ($T_{\text{operation}} \approx 800 - 1900 \text{ K}$)⁹³⁻⁹⁵. In these high temperature applications, thermal effects will populate metastable configurations and could also affect the predicted position of the defect charge transition level (i.e., non-

negligible entropic term of $T \times [s_f(q, T) - s_f(q', T)] / (q - q')$ — especially when the change in charge state leads to significant differences in the defect structure and symmetry, spin state and position of the defect level within the bandgap.⁸⁰ Finally, we note the promise of machine learning force fields for defects. By learning the defect energy surface, they reduce the cost of modelling defect dynamics at the device operating temperature and on larger time and length scales, which can be key to predict complex processes like defect reactions or diffusion⁹⁶.

IV. METHODOLOGY

Density Functional Theory calculations. All reference calculations were performed with Density Functional Theory using the exchange-correlation functional PBEsol⁹⁷ and the projector augmented wave method⁹⁸, as implemented in the Vienna Ab initio Simulation Package (VASP)^{99,100}. We used the standard PAW PBE potentials (version 64) for Te ($5s^25p^4$) and Cd ($4d^{10}5s^2$). Although hybrid functionals are typically required to accurately model the electronic behaviour of defects, we used a more affordable GGA functional for several reasons: i) PBEsol has been found to accurately describe the vibrational properties of crystals¹⁰¹; ii) it correctly identifies the same defect configurations reported in a previous study using the HSE06 hybrid functional¹²; and iii) we aimed to benchmark how to properly train defect MLFFs to reach the high accuracies required to estimate g_f , and as a result needed a functional that would allow a thorough exploration of the configurational landscape up to the CdTe synthesis temperature.

We converged the plane wave energy cutoff and Γ -centered k-point mesh to 1 meV/atom, resulting in values of 450 eV and $4 \times 4 \times 4$ for the conventional cell of CdTe. To minimise Pulay stress errors during molecular dynamics simulations, we increased the converged energy cutoff by 30% (585 eV). The threshold for electronic convergence was set to 10^{-5} eV.

Training of machine learning force fields. We used the structure similarity kernel in VASP to generate the training sets of configurations using its on-the-fly molecular dynamics

approach^{102–105}. This involved heating runs performed under the NPT ensemble with a pressure of 1 atm and from an initial temperature of 100 K up to 30% above our target temperature of 840 K. In addition, we generated a series of compressed and expanded structures (0.9–1.1 of the original cell volume) to ensure that the model could be used for the quasiharmonic approximation. For bulk CdTe and its defects, we used a $2 \times 2 \times 2$ supercell of the conventional cell (13.0 Å in length and 64 atoms for bulk CdTe). For Te, we included all the low-energy phases available in the Materials Project¹⁰⁶ ($E_{hull} \leq k_B T_{synthesis} = k_B \times (840 \text{ K}) = 0.08 \text{ eV}$), which were expanded to cubic supercells of at least 10 Å in length. For the liquid Te phase, we generated two models with the `packmol` code¹⁰⁷: two cubic boxes of 15 Å and 17.5 Å in length, containing 95 and 220 atoms, respectively, which gave densities matching the reported values in previous studies at our target temperatures ($\rho = 0.027 \text{ atoms}/\text{Å}^3$)¹⁰⁸.

An independent model was trained for each system (bulk CdTe, Te_i^{+1} , V_{Te}^{+2} and Te) since this lead to higher accuracy models than training one *joint* model on the bulk and defect datasets. However, we have observed that training a model *only* on defect configurations should be avoided if the model will be applied to study the absolute energies of larger system sizes (e.g., defect formation energies). While models selectively trained on defect configurations achieve higher accuracy for defective supercells with the *same number of atoms*, these models lead to a *systematic* error in the total energies of *larger supercells* than the supercells used for training, as explained in detail in Supplementary Section 1 C.

After generating the training sets with VASP, we trained MACE⁸³ force fields on these datasets to obtain models with higher accuracy and speed. 10% of the configurations in these datasets were used as validation sets to monitor the loss during training. We used a MACE model with Ziegler-Biersack-Littmark (ZBL) pair repulsion¹⁰⁹, 2 message passing layers, 256 invariant messages, correlation order of 3, angular resolution of 3 and cutoff radius of 5 Å. The batch size was set to 2 and the Huber loss function was used, with weights of 1, 100 and 100 for the mean square errors in the energies, forces and stresses, respectively. For the last 20% of the training epochs, the weights were updated to values of 1000, 10 and 100 for energy, force and stress, respectively — following the recommended strategy of increasing the

weight on the energy errors during the final training epochs. The models were trained until the validation loss converged, which required around 150-200 epochs. The reference energies were defined as the potential energies of isolated Cd and Te atoms.

Validation of machine learning force fields. To generate the test sets, we performed NPT molecular dynamics simulations with the trained models at three different temperatures (300, 550 and 900 K), running five independent 24 ps runs at each temperature. We then sampled 100-300 equally-spaced configurations from these trajectories, and performed DFT calculations on them, which were used to calculate the MAE and RMSE of each model (see distribution of sampled configurations and associated errors in Figs. [Supplementary Figure S1](#) to [Supplementary Figure S5](#)). The MAE and RMSE for the forces and stresses were calculated component wise, as defined in Ref. [110](#). In addition, we also validated that the model successfully described the phonons and vibrational free energy of bulk CdTe (see [Supplementary Figure S6](#)).

Defect calculations. Defect calculations were setup and analysed using `doped`⁹². To account for spurious finite-size supercell effects, the Kumagai-Oba¹¹¹ (eFNV) charge correction scheme was used to calculate E_{corr} , as automated in `doped`. The Fermi level was assumed to be located in the middle of the band gap.

Spin degeneracy. The spin degeneracy was calculated with `doped` using

$$\Omega^{\text{spin}} = \frac{Z_d^{\text{spin}}}{Z_b^{\text{spin}}} = 2S + 1 \quad (5)$$

where Z denotes the partition function and S the total spin angular momentum. For example, Te_i^{+1} has one unpaired electron, resulting in $\Omega^{\text{spin}} = 2 \times (1/2) + 1 = 2$. This degeneracy factor Ω can be converted into its respective formation entropy using $s_f = k_B \ln(\Omega)$ ², where k_B denotes the Boltzmann constant.

Orientalional degeneracy. The orientational degeneracy was also calculated with `doped` using

$$\Omega^{\text{orient}} = \frac{Z_d^{\text{orient}}}{Z_b^{\text{orient}}} = \frac{N_b}{N_d} \quad (6)$$

where N is the number of symmetry operations of the defect site in the bulk (b) and defective (d) supercells². As discussed in the `doped` documentation⁹², for vacancies and substitutions there is a clear definition of the defect site in the pristine supercell (e.g., the lattice site where the vacancy/substitution forms). In contrast, for interstitials, the definition of the lattice site in the bulk can be ambiguous, which affects the *partition* between orientational degeneracy and site multiplicity. Here, we follow the definition adopted by Kavanagh *et al*⁹², where the interstitial site in the *bulk* is defined as the *relaxed* site of the interstitial but with all other atoms fixed in their *bulk* (unrelaxed) positions, while the interstitial site in the *defect* supercell corresponds to the relaxed position of *both* the interstitial and all other atoms. Accordingly, the site multiplicity is determined for the lattice site that the interstitial occupies after relaxation and with all other atoms fixed in their bulk positions. Note that other definitions can be adopted and will lead to the *same total* prefactor ($\Omega^{\text{orient}} \times N_{\text{site}}$) but different *partitions* into the orientational and site degeneracies.

For Te_i^{+1} , the C_{2v} configuration has an initial site symmetry of C_s which becomes C_{2v} when the atoms around the interstitial relax due to the formation of the Te-Te dimer. Similarly, the (metastable) C_s configuration has an initial C_1 site symmetry which becomes C_s after the relaxation. As a result, for both configurations the orientational degeneracy Ω^{orient} is 0.5 (e.g. the site symmetry increases upon relaxation of the atoms around the interstitial). The site multiplicities per primitive cell are 12 and 24 for the C_{2v} and C_s configurations, respectively. These degeneracies are accounted for when predicting the defect concentration (Eq. (4)) where the orientational entropy is included in g_f .

Electronic entropy. The electronic entropy was calculated using the fixed density of states (DOS) approximation^{56,112–115}, that assumes a temperature-independent DOS. Since the electronic entropy is sensitive to the bandgap, and PBEsol significantly underestimates it, we performed self-consistent field HSE06 ($\alpha = 0.345$ ¹³) calculations on the 0 K structures optimised with PBEsol. The electronic entropy is then calculated using

$$S^{\text{elec}} = -\gamma k_B \int_{-\infty}^{\infty} D(E) (f(E, T) \ln(f(E, T)) + (1 - f(E, T)) \ln(1 - f(E, T))) dE \quad (7)$$

where γ equals 1 for spin-polarized systems and 2 for spin-unpolarized systems.¹¹³ $D(E)$ is the electronic density of states at energy E (calculated at 0 K) and $f(E)$ is the occupation of the energy level E given by Fermi-Dirac occupation statistics

$$f(E, T) = \left(\exp\left(\frac{E - E_F}{k_B T}\right) + 1 \right)^{-1} \quad (8)$$

with E_F denoting the Fermi level. We define the formation electronic entropy as the entropy change in the reaction $(\text{CdTe})_{32} + \text{Te} \rightarrow \text{Cd}_{32}\text{Te}_{33}^{+1} + e^-$ (Supplementary Figure S17), with E_F for each of these terms calculated as follows:

- Te, CdTe and $\text{Cd}_{32}\text{Te}_{33}^{+1}$: The Fermi level is assumed to be located mid-gap between the highest occupied and lowest unoccupied state. Note that, in theory, the Fermi level of CdTe should correspond to the *self-consistent* value determined for a set of defects and charge states^{116,117}, but in practice this is currently not feasible, and assuming the level to be midgap is a reasonable approximation in this study³⁸. Te_i^{+1} introduces an empty state 0.75 eV above the valence band maximum (VBM), and thus E_F is set to $0.75/2 = 0.37$ eV above the VBM. Note that the electronic entropy is sensitive to the energy difference between E_F and the lowest unoccupied state, thus requiring an accurate electronic structure.
- Extra electron: It is defined as the excess electronic entropy when one extra electron is added to the conduction band minimum (CBM) of the bulk system, i.e. $s^{\text{elec}}(N + 1) - s^{\text{elec}}(N)$, where $s^{\text{elec}}(N)$ denotes the electronic entropy of bulk CdTe with N and $N + 1$ electrons. To calculate the electronic entropy of the $N + 1$ system, we determine E_F with¹¹⁸

$$E_F = E_{CBM} + k_B T \ln\left(\frac{n}{N_C}\right) \quad (9)$$

where N_C denotes the effective density of states in the conduction band, given by

$$N_c = 2 \left(\frac{2\pi m_e^* k_B T}{h^2} \right)^{3/2} \quad (10)$$

with m_e^* and h representing the electron effective mass and Planck constant, respectively. For the concentration of excess electrons donated by the defect, n , we assume a value of $n = 10^{15} \text{ cm}^{-3}$ in the dilute limit of defect formation.

Finally, we note that the electronic entropy can become significant at elevated temperatures ($T \geq 1000 \text{ K}$, [Supplementary Figure S17](#)) if the defect i) introduces an (occupied) empty state close to the (CBM) VBM or ii) changes the occupation of localised d/f bands of nearby cations (e.g., V_O^{+2} reducing two Ce^{+4} to Ce^{+3} in CeO_2), as demonstrated in previous studies.^{93,119}

Structural entropy. The code `ShakeNBreak` was used to identify the defect ground state and metastable configurations.^{4,5,85} From these configurations, the structural or configurational entropy can be estimated using

$$s_f^{struc} = -k_B \sum_i p_i \ln(p_i) \quad (11)$$

where p_i denotes the Boltzmann probability of configuration i , given by

$$p_i = \frac{e^{-\frac{G_i}{k_B T}}}{\sum_j e^{-\frac{G_j}{k_B T}}} = \frac{\Omega_i^{elec} \Omega_i^{spin} \Omega_i^{orient} \Omega_i^{vib} e^{-\frac{U_i}{k_B T}}}{\sum_j \Omega_j^{elec} \Omega_j^{spin} \Omega_j^{orient} \Omega_j^{vib} e^{-\frac{U_j}{k_B T}}} \quad (12)$$

where G_i and U_i are the Gibbs free energy and internal energy of configuration i , and we have included the degeneracy factors Ω since these can be configuration dependent. In practice, the main degrees of freedom that change between configurations are the orientational and spin (and vibrational to a lower extent), thus simplifying Eq. (12) to

$$p_i = \frac{\Omega_i^{spin} \Omega_i^{orient} e^{-\frac{U_i - TS_i^{vib}}{k_B T}}}{\sum_j \Omega_j^{spin} \Omega_j^{orient} e^{-\frac{U_j - TS_j^{vib}}{k_B T}}}. \quad (13)$$

Beyond applying this analytical approach, we also calculated the structural entropy using the ‘inherent structures’ method (IS).²⁵ Within this formalism, we performed NPT MD

trajectories at 30 temperatures (equally spaced ranging from 100 to 840 K), then sampled 1600 equally-spaced configurations and performed conjugate gradient optimisations to quench the structures to the nearest local minima in the 0 K PES (Supplementary Figure S16). The configurational entropy was then calculated with

$$s_f^{struc} = s_f^{struc}(T_i) + \int_{T_i}^{T_f} \frac{1}{T} \frac{\partial \langle e_{IS}^V(T) \rangle}{\partial T} dT. \quad (14)$$

where $\langle e_{IS}^V(T) \rangle$ denotes the average potential energy of the inherent structures sampled at T , with the volume fixed to the optimal value for the 0 K ground state structure, and T_i and T_f set to 100 and 840 K, respectively. This method resulted in $s_f^{struc}(840 \text{ K}) = 1.05 k_B$, in the same order of the value of $0.6 k_B$ obtained with the analytical method. The slightly larger value of s_f^{struc} estimated with the IS formalism likely stems from the additional intermediate configurations sampled with quenching.

Finally, a third approach to account for the structural entropy involves coarse-graining the configurational degree of freedom, and calculating the total defect concentration as a sum over the different configurations i using²

$$c = \sum_i c_i = \sum_i \frac{N_i}{V} \exp\left(-\frac{g_{f,i}}{k_B T}\right) \quad (15)$$

where N_i and $g_{f,i}$ denote the number of symmetry-equivalent sites and formation free energy of configuration i (with $g_{f,i} = u_{f,i} - T(s_{f,i}^{vib,harm} + s_{f,i}^{orient} + s_{f,i}^{spin} + s_{f,i}^{elec})$). From this expression, an effective formation free energy can be obtained by

$$g_{eff} = -k_B T \ln\left(\frac{V}{N} c\right) \quad (16)$$

where N denotes the number of symmetry-equivalent sites for the ground state structure. By comparing g_{eff} with the g_f calculated using Eq. (11), we verified that these values agree (see Supplementary Figure S18).

Vibrational entropy. The harmonic and quasiharmonic vibrational free energies were calculated using phonopy^{86,120}. Within the quasiharmonic framework, which includes the

effect of thermal expansion on the phonon frequencies, we generated 11 structures by scaling the supercell volume by factors ranging from 0.9 to 1.10 with a 0.02 increment.

Thermodynamic integration. Fully anharmonic free energies were calculated using non-equilibrium TI in LAMMPS^{121,122}, as implemented in the code calphy⁸¹. This involved two thermodynamic integration paths: first, we integrate from the Einstein crystal to the anharmonic one at 100 K (Frenkel Ladd method) and then we calculate the temperature variation of the free energy at constant pressure by integrating from 100 K to 840 K (commonly known as reversible scaling). These simulations were performed fixing the center of mass, as done in previous studies^{18,81,122}. For each path, we performed 10 independent TI runs to estimate the error, defined as the standard error of the mean free energy ($\sigma_\mu = \sigma/\sqrt{N}$, where σ denotes the standard deviation in the individual free energies calculated from the $N = 10$ independent TI runs). The switching time was adjusted for each system until the error converged to an acceptable value (see [Supplementary Figure S15](#)), which must be very low ($\sigma_\mu < 0.25$ meV/atom ≈ 20 meV/supercell) to get an accurate g_f . Since g_f is the difference between two large and similar numbers (the free energies of the bulk and defect supercells), small relative errors in either of these quantities can lead to a large error in g_f . The convergence tests resulted in the switching times reported in [TABLE II](#).

TABLE II Equilibration and switching times in picoseconds used for the thermodynamic integration paths of each system involved in the defect formation reaction. The timestep was set to 2 fs.

Path	CdTe	Te _i ⁺¹	V _{Te} ⁺²	Te
Einstein → Anharmonic	25, 100	25, 200	15, 150	25, 70
100 K → 840 K	25, 170	25, 1000	25, 1000	25, 70
840 K → 500 K	-	-	-	25, 70

We note that during the temperature scaling runs of the interstitial, defect diffusion occurs within the simulation timescale. This migration, which arises from the shape of the

potential energy surface, contributes to the anharmonic free energy through the sampling of intermediate structures during site hopping. We expect that their contribution is small as the defects spend more time around their local minima configurations.

Finally, calculating the temperature dependence of the free energy for tellurium is slightly more challenging since it melts at 722 K¹²³. Accordingly, we performed two TI simulations⁸¹: i) Einstein crystal (100 K) \rightarrow Anharmonic crystal (100 K) \rightarrow Anharmonic crystal (840 K) and ii) Uhlenbeck-Ford model (840 K) \rightarrow Liquid Te (840 K) \rightarrow Liquid Te (500 K). By comparing the free energies from both simulations, we determined the phase transition temperature and the variation of the free energy with temperature (Supplementary Figure S19). The calculated phase transition temperature is 704 K, which is in good agreement with the experimentally reported value of 722 K¹²³.

Molecular dynamics. To model the behaviour of the defects at room temperature, we performed NPT molecular dynamics with LAMMPS¹²¹ using both a 65-atom ($a = 13 \text{ \AA}$) and 513-atom cubic supercells ($a = 26 \text{ \AA}$) to properly capture the dynamics and diffusion of the interstitial. The Nosé-Hoover thermostat and barostat were used (1 atm, 300 K and timestep of 2 fs) with equilibration and production times of 300 ps and 1 ns, respectively. These trajectories were analysed with Python using tools from the ase¹²⁴, pymatgen-analysis-defects^{125,126}, pymatgen¹²⁷⁻¹²⁹, dscribe^{130,131}, umap¹³², direct¹³³, matplotlib¹³⁴, and seaborn¹³⁵ packages, and visualised with Ovito¹³⁶ and CrystalMaker¹³⁷.

The energy barriers for the changes in configuration, orientation and position of Te_i^{+1} were calculated with the Nudge Elastic Band method^{138,139}, as implemented in ase.¹²⁴ The associated rates for these processes were calculated using Transition State Theory (e.g. $k(T) = \nu \exp(-E_b/(k_B T))$) and approximating the attempt frequency ν by the curvature of the PES at the initial state. The anharmonicity scores were calculated with FHI-vibes^{87,140} on MD trajectories (NPT ensemble; 1 atm, 500 ps) at three temperatures (300, 550 and 900 K) for pristine CdTe and Te_i^{+1} .

DECLARATIONS

Data availability. The datasets and trained models will be available from a Zenodo repository upon publication.

Acknowledgments. We thank Seán R. Kavanagh for suggesting Te_1^{+1} as a test system and discussions regarding metastability. We also thank Venkat Kamil, Maurice de Koning, Talid Sinno, Blazej Grabowski, Sarath Menon and Luciano Colombo for useful discussions about thermodynamic integration. I.M.-L. thanks Imperial College London (ICL) for funding a President’s PhD scholarship. J.K. acknowledges support from the Swedish Research Council (VR) program 2021-00486. We are grateful to the UK Materials and Molecular Modelling Hub for computational resources, which is partially funded by EPSRC (EP/P020194/1 and EP/T022213/1). This work used the ARCHER2 UK National Supercomputing Service (<https://www.archer2.ac.uk>) via our membership of the UK’s HEC Materials Chemistry Consortium, funded by EPSRC (EP/L000202). We acknowledge the ICL High Performance Computing services for computational resources.

Author contributions. Conceptualisation & Project Administration: A.W., I.M.-L. Investigation, methodology and formal analysis: I.M.-L. Supervision: A.W. Writing - original draft: I.M.-L. Writing - review & editing: All authors. Resources and funding acquisition: A.W. These author contributions are defined according to the CRediT contributor roles taxonomy.

Competing interests. The authors declare no competing interests.

REFERENCES

- ¹A. M. Stoneham, *Theory of defects in solids*, Oxford University Press, 1975.
- ²I. Mosquera-Lois, S. R. Kavanagh, J. Klarbring, K. Tolborg and A. Walsh, *Chem. Soc. Rev.*, 2023, **52**, 5812–5826.
- ³C. Freysoldt, B. Grabowski, T. Hickel, J. Neugebauer, G. Kresse, A. Janotti and C. G.

- Van De Walle, *Rev. Mod. Phys.*, 2014, **86**, 253–305.
- ⁴I. Mosquera-Lois, S. R. Kavanagh, A. Walsh and D. O. Scanlon, *npj Comput. Mater.*, 2023, **9**, 1–11.
- ⁵I. Mosquera-Lois and S. R. Kavanagh, *Matter*, 2021, **4**, 2602–2605.
- ⁶X. Wang, S. R. Kavanagh, D. O. Scanlon and A. Walsh, *Phys. Rev. B*, 2023, **108**, 134102.
- ⁷X. Wang, S. R. Kavanagh and A. Walsh, *ACS Energy Lett.*, 0, **0**, 161–167.
- ⁸X. Wang, S. R. Kavanagh, D. O. Scanlon and A. Walsh, *Joule*, 2024, 2105–2122.
- ⁹A. G. Squires, L. Ganeshkumar, C. N. Savory, S. R. Kavanagh and D. O. Scanlon, *ACS Energy Lett.*, 2024, **9**, 4180–4187.
- ¹⁰J.-H. Yang, L. Shi, L.-W. Wang and S.-H. Wei, *Sci Rep*, 2016, **6**, 21712.
- ¹¹A. Alkauskas, C. E. Dreyer, J. L. Lyons and C. G. Van de Walle, *Phys. Rev. B*, 2016, **93**, 201304.
- ¹²S. R. Kavanagh, D. O. Scanlon, A. Walsh and C. Freysoldt, *Faraday Discuss.*, 2022, **239**, 339–356.
- ¹³S. R. Kavanagh, A. Walsh and D. O. Scanlon, *ACS Energy Lett.*, 2021, 1392–1398.
- ¹⁴S. R. Kavanagh, R. S. Nielsen, J. L. Hansen, R. S. Davidsen, O. Hansen, A. E. Samli, P. C. Vesborg, D. O. Scanlon and A. Walsh, *Intrinsic point defect tolerance in selenium for indoor and tandem photovoltaics*, Preprint at 10.26434/chemrxiv-2024-91h02 (2024).
- ¹⁵D. Guo, C. Qiu, K. Yang and H.-X. Deng, *Phys. Rev. Appl.*, 2021, **15**, 064025.
- ¹⁶W. B. Fowler, M. Stavola, A. Venzie and A. Portoff, *J. Appl. Phys.*, 2024, **135**, 170901.
- ¹⁷A. S. Bochkarev, A. van Roekeghem, S. Mossa and N. Mingo, *Phys. Rev. Materials*, 2019, **3**, 093803.
- ¹⁸B. Cheng and M. Ceriotti, *Phys. Rev. B*, 2018, **97**, 054102.
- ¹⁹S. Chiesa, P. M. Derlet and S. L. Dudarev, *Phys. Rev. B*, 2009, **79**, 214109.
- ²⁰M. de Koning, C. R. Miranda and A. Antonelli, *Phys. Rev. B*, 2002, **66**, 104110.
- ²¹M. De Koning, S. Ramos De Debiaggi and A. Monti, *DDF*, 2003, **224-225**, 59–74.
- ²²A. Glensk, B. Grabowski, T. Hickel and J. Neugebauer, *Phys. Rev. X*, 2014, **4**, 011018.
- ²³B. Grabowski, L. Ismer, T. Hickel and J. Neugebauer, *Phys. Rev. B*, 2009, **79**, 134106.

- ²⁴G. Lucas and R. Schäublin, *Nucl. Instrum. Methods Phys. Res.*, 2009, **267**, 3009–3012.
- ²⁵J. Luo, C. Zhou, Y. Cheng, Q. Li, L. Liu, J. F. Douglas and T. Sinno, *Phys. Rev. Mater.*, 2022, **6**, 064603.
- ²⁶T. A. Mellan, A. I. Duff, B. Grabowski and M. W. Finnis, *Phys. Rev. B*, 2019, **100**, 024303.
- ²⁷E. V. Safonova, Y. P. Mitrofanov, R. A. Konchakov, A. Y. Vinogradov, N. P. Kobelev and V. A. Khonik, *J. Phys.: Condens. Matter*, 2016, **28**, 215401.
- ²⁸A. Satta, F. Willaime and S. de Gironcoli, *Phys. Rev. B*, 1998, **57**, 11184–11192.
- ²⁹G. S. Smirnov and V. V. Stegailov, *J. Phys.: Condens. Matter*, 2019, **31**, 235704.
- ³⁰D. Shin and C. Wolverton, *Acta Mater.*, 2012, **60**, 5135–5142.
- ³¹Y. Gong, B. Grabowski, A. Glensk, F. Körmann, J. Neugebauer and R. C. Reed, *Phys. Rev. B*, 2018, **97**, 214106.
- ³²D. Smirnova, S. Starikov, G. D. Leines, Y. Liang, N. Wang, M. N. Popov, I. A. Abrikosov, D. G. Sangiovanni, R. Drautz and M. Mrovec, *Phys. Rev. Mater.*, 2020, **4**, 013605.
- ³³X. Zhang, B. Grabowski, T. Hickel and J. Neugebauer, *Comput. Mater. Sci.*, 2018, **148**, 249–259.
- ³⁴L. Mathes, T. Gigl, M. Leitner and C. Hugenschmidt, *Phys. Rev. B*, 2020, **101**, 134105.
- ³⁵T. Sinno, Z. K. Jiang and R. A. Brown, *Appl. Phys. Lett.*, 1996, **68**, 3028–3030.
- ³⁶O. K. Al-Mushadani and R. J. Needs, *Phys. Rev. B*, 2003, **68**, 235205.
- ³⁷E. Rauls and T. Frauenheim, *Phys. Rev. B*, 2004, **69**, 155213.
- ³⁸P. E. Blöchl, E. Smargiassi, R. Car, D. B. Laks, W. Andreoni and S. T. Pantelides, *Phys. Rev. Lett.*, 1993, **70**, 2435–2438.
- ³⁹D. Maroudas and R. A. Brown, *Phys. Rev. B*, 1993, **47**, 15562–15577.
- ⁴⁰M. I. Mendeleev and Y. Mishin, *Phys. Rev. B*, 2009, **80**, 144111.
- ⁴¹P. J. Ungar, T. Halicioglu and W. A. Tiller, *Phys. Rev. B*, 1994, **50**, 7344–7357.
- ⁴²P. Wynblatt, *J. Phys. Chem. Solids*, 1969, **30**, 2201–2211.
- ⁴³J. H. Harding, *Physica B+C*, 1985, **131**, 13–26.
- ⁴⁴J. H. Harding and A. M. Stoneham, *Philos. Mag. B*, 1981, **43**, 705–713.
- ⁴⁵J. H. Harding, *Phys. Rev. B*, 1985, **32**, 6861.

- ⁴⁶J. Luo, C. Zhou, Q. Li and L. Liu, *J. Chem. Phys.*, 2022, **156**, 214113.
- ⁴⁷J. Luo, C. Zhou, Q. Li and L. Liu, *Materials*, 2022, **15**, 4026.
- ⁴⁸Y. Mishin, M. R. Sorensen and A. F. Voter, *Philos. Mag. A*, 2001, **81**, 2591–2612.
- ⁴⁹P. Wynblatt, *Phys. Status Solidi B*, 1969, **36**, 797–808.
- ⁵⁰C. Lapointe, T. D. Swinburne, L. Proville, C. S. Becquart, N. Mousseau and M.-C. Marinica, *Phys. Rev. Mater.*, 2022, **6**, 113803.
- ⁵¹P. W. M. Jacobs, *J. Chem. Soc., Faraday Trans.*, 1990, **86**, 1197–1201.
- ⁵²J. Nam and R. Gómez-Bombarelli, *Interpolation and differentiation of alchemical degrees of freedom in machine learning interatomic potentials*, Preprint at <http://arxiv.org/abs/2404.10746> (2024).
- ⁵³S. Ramos de Debiaggi, M. de Koning and A. M. Monti, *Phys. Rev. B*, 2006, **73**, 104103.
- ⁵⁴K. M. Carling, G. Wahnström, T. R. Mattsson, N. Sandberg and G. Grimvall, *Phys. Rev. B*, 2003, **67**, 054101.
- ⁵⁵S. M. Foiles, *Phys. Rev. B*, 1994, **49**, 14930–14938.
- ⁵⁶S. K. Estreicher, M. Sanati, D. West and F. Ruymgaart, *Phys. Rev. B*, 2004, **70**, 125209.
- ⁵⁷M. Sanati and S. K. Estreicher, *Phys. B: Condens. Matter*, 2003, **340–342**, 630–636.
- ⁵⁸M. Sanati and S. K. Estreicher, *Solid State Commun.*, 2003, **128**, 181–185.
- ⁵⁹M. Sanati and S. K. Estreicher, *Phys. Rev. B*, 2005, **72**, 165206.
- ⁶⁰E. Smargiassi and R. Car, *Phys. Rev. B*, 1996, **53**, 9760–9763.
- ⁶¹C. Catlow, J. Corish, P. Jacobs and A. Lidiard, *J. Phys. C: Sol. Stat. Phys.*, 1981, **14**, L121.
- ⁶²P. Ágoston and K. Albe, *Phys. Chem. Chem. Phys.*, 2009, **11**, 3226–3232.
- ⁶³T. Zacherle, P. C. Schmidt and M. Martin, *Phys. Rev. B*, 2013, **87**, 235206.
- ⁶⁴T. Smith, S. Moxon, J. S. Tse, J. M. Skelton, D. J. Cooke, L. J. Gillie, E. L. d. Silva, R. M. Harker, M. T. Storr, S. C. Parker and M. Molinari, *J. Phys. Energy*, 2023, **5**, 025004.
- ⁶⁵T. Zacherle, A. Schrieffer, R. A. De Souza and M. Martin, *Phys. Rev. B*, 2013, **87**, 134104.
- ⁶⁶A. Walsh, A. A. Sokol and C. R. A. Catlow, *Phys. Rev. B Condens. Matter*, 2011, **83**, 224105.

- ⁶⁷B. Baldassarri, J. He and C. Wolverton, *Phys. Rev. Mater.*, 2024, **8**, 055407.
- ⁶⁸S. L. Millican, J. M. Clary, C. B. Musgrave and S. Lany, *Chem. Mater.*, 2022, **34**, 519–528.
- ⁶⁹S. Moxon, J. Skelton, J. S. Tse, J. Flitcroft, A. Togo, D. J. Cooke, E. L. d. Silva, R. M. Harker, M. T. Storr, S. C. Parker and M. Molinari, *J. Mater. Chem. A*, 2022, **10**, 1861–1875.
- ⁷⁰Y. Sun, T. Liu, Q. Chang and C. Ma, *J. Phys. Chem. Solids*, 2018, **115**, 228–232.
- ⁷¹G. Miceli and A. Pasquarello, *Phys. Rev. B*, 2016, **93**, 165207.
- ⁷²S. Grieshammer, T. Zacherle and M. Martin, *Phys. Chem. Chem. Phys.*, 2013, **15**, 15935–15942.
- ⁷³C. Cazorla, *Phys. Rev. Appl.*, 2017, **7**, 044025.
- ⁷⁴J. M. Wynn, R. J. Needs and A. J. Morris, *Structures and finite-temperature abundances of defects in In_2O_3-II from first-principles calculations*, Preprint at <https://arxiv.org/abs/1609.04760> (2016).
- ⁷⁵M. Youssef and B. Yildiz, *Phys. Rev. B*, 2012, **86**, 144109.
- ⁷⁶L. N. Holtzman, P. A. Vargas, R. G. Hennig and K. Barmak, *J. Chem. Phys.*, 2024, **161**, 144105.
- ⁷⁷A. Gorfer, R. Abart and C. Dellago, *Phys. Rev. Mater.*, 2024, **8**, 073602.
- ⁷⁸R. J. Tarento and J. H. Harding, *J. Phys. C: Solid State Phys.*, 1987, **20**, L677.
- ⁷⁹C. Zhang, F. Gygi and G. Galli, *Phys. Rev. Mater.*, 2024, **8**, 046201.
- ⁸⁰T. S. Bjørheim, M. Arrigoni, D. Gryaznov, E. Kotomin and J. Maier, *Phys Chem Chem Phys*, 2015, **17**, 20765–20774.
- ⁸¹S. Menon, Y. Lysogorskiy, J. Rogal and R. Drautz, *Phys. Rev. Mater.*, 2021, **5**, 103801.
- ⁸²V. Kapil, E. Engel, M. Rossi and M. Ceriotti, *J. Chem. Theory Comput.*, 2019, **15**, 5845–5857.
- ⁸³I. Batatia, D. P. Kovacs, G. Simm, C. Ortner and G. Csanyi, *Adv Neural Inf Process Syst*, 2022, **35**, 11423–11436.
- ⁸⁴W. K. Metzger, S. Grover, D. Lu, E. Colegrove, J. Moseley, C. L. Perkins, X. Li, R. Mallick, W. Zhang, R. Malik, J. Kephart, C.-S. Jiang, D. Kuciauskas, D. S. Albin, M. M. Al-Jassim, G. Xiong and M. Gloeckler, *Nat Energy*, 2019, **4**, 837–845.

- ⁸⁵I. Mosquera-Lois, S. R. Kavanagh, A. Walsh and D. O. Scanlon, *J. Open Source Softw.*, 2022, **7**, 4817.
- ⁸⁶A. Togo, L. Chaput, T. Tadano and I. Tanaka, *J. Phys. Condens. Matter*, 2023, **35**, 353001.
- ⁸⁷F. Knoop, T. A. R. Purcell, M. Scheffler and C. Carbogno, *Phys. Rev. Mater.*, 2020, **4**, 083809.
- ⁸⁸M. Choi, F. Oba, Y. Kumagai and I. Tanaka, *Adv. Mater.*, 2013, **25**, 86–90.
- ⁸⁹J. Park, B. Xu, J. Pan, D. Zhang, S. Lany, X. Liu, J. Luo and Y. Qi, *npj Comput Mater*, 2023, **9**, 1–13.
- ⁹⁰I. Mosquera-Lois, S. R. Kavanagh, A. M. Ganose and A. Walsh, *npj Comput Mater*, 2024, **10**, 1–9.
- ⁹¹L. D. Whalley, *J. Phys. Chem. C.*, 2023, **127**, 15738–15746.
- ⁹²S. R. Kavanagh, A. G. Squires, A. Nicolson, I. Mosquera-Lois, A. M. Ganose, B. Zhu, K. Brlec, A. Walsh and D. O. Scanlon, *J. Open Source Softw.*, 2024, **9**, 6433.
- ⁹³S. S. Naghavi, A. A. Emery, H. A. Hansen, F. Zhou, V. Ozolins and C. Wolverton, *Nat Commun*, 2017, **8**, 285.
- ⁹⁴D. Sikstrom and V. Thangadurai, *Ionics*, 2024, **1**, 1.
- ⁹⁵J. Gao, G. Tian, A. Sornioti, A. E. Karci and R. Di Palo, *Appl. Therm. Eng.*, 2019, **147**, 177–187.
- ⁹⁶X. Zhong, F. Höfling and T. John, *Hydrogen diffusion in garnet: insights from atomistic simulations*, Preprint at <http://arxiv.org/abs/2410.07724> (2024).
- ⁹⁷J. P. Perdew, A. Ruzsinszky, G. I. Csonka, O. A. Vydrov, G. E. Scuseria, L. A. Constantin, X. Zhou and K. Burke, *Phys. Rev. Lett.*, 2008, **100**, 136406.
- ⁹⁸G. Kresse and J. Furthmüller, *Comput. Mater. Sci.*, 1996, **6**, 15–50.
- ⁹⁹G. Kresse and J. Hafner, *Phys. Rev. B*, 1993, **47**, 558–561.
- ¹⁰⁰G. Kresse and J. Hafner, *Phys. Rev. B*, 1994, **49**, 14251–14269.
- ¹⁰¹J. M. Skelton, D. Tiana, S. C. Parker, A. Togo, I. Tanaka and A. Walsh, *J. Chem. Phys.*, 2015, **143**, 064710.
- ¹⁰²R. Jinnouchi, J. Lahnsteiner, F. Karsai, G. Kresse and M. Bokdam, *Phys. Rev. Lett.*, 2019,

- 122**, 225701.
- ¹⁰³R. Jinnouchi, F. Karsai and G. Kresse, *Phys. Rev. B*, 2019, **100**, 014105.
- ¹⁰⁴R. Jinnouchi, K. Miwa, F. Karsai, G. Kresse and R. Asahi, *J. Phys. Chem. Lett.*, 2020, **11**, 6946–6955.
- ¹⁰⁵P. Liu, C. Verdi, F. Karsai and G. Kresse, *Phys. Rev. B*, 2022, **105**, L060102.
- ¹⁰⁶A. Jain, S. P. Ong, G. Hautier, W. Chen, W. D. Richards, S. Dacek, S. Cholia, D. Gunter, D. Skinner, G. Ceder and K. A. Persson, *APL Materials*, 2013, **1**, 011002.
- ¹⁰⁷L. Martínez, R. Andrade, E. G. Birgin and J. M. Martínez, *J Comput Chem*, 2009, **30**, 2157–2164.
- ¹⁰⁸J. Akola, R. O. Jones, S. Kohara, T. Usuki and E. Bychkov, *Phys. Rev. B*, 2010, **81**, 094202.
- ¹⁰⁹J. F. Ziegler and J. P. Biersack, in *The Stopping and Range of Ions in Matter*, ed. D. A. Bromley, Springer US, Boston, MA, 1985, pp. 93–129.
- ¹¹⁰J. D. Morrow, J. L. A. Gardner and V. L. Deringer, *J. Chem. Phys.*, 2023, **158**, 121501.
- ¹¹¹Y. Kumagai and F. Oba, *Phys. Rev. B Condens. Matter*, 2014, **89**, 195205.
- ¹¹²O. Eriksson, J. M. Wills and D. Wallace, *Phys. Rev. B*, 1992, **46**, 5221–5228.
- ¹¹³X. Zhang, B. Grabowski, F. Körmann, C. Freysoldt and J. Neugebauer, *Phys. Rev. B*, 2017, **95**, 165126.
- ¹¹⁴A. Metsue, A. Oudriss, J. Bouhattate and X. Feaugas, *J. Chem. Phys.*, 2014, **140**, 104705.
- ¹¹⁵F. Willaime, A. Satta, M. Nastar and O. Le Bacq, *Int. J. Quantum Chem.*, 2000, **77**, 927–939.
- ¹¹⁶A. G. Squires, D. O. Scanlon and B. J. Morgan, *J. Open Source Softw.*, 2023, **8**, 4962.
- ¹¹⁷J. Buckeridge, *Comput. Phys. Commun.*, 2019, **244**, 329–342.
- ¹¹⁸A. H. M. Smets, K. Jäger, O. Isabella, R. A. v. Swaaij and M. Zeman, *Solar energy : the physics and engineering of photovoltaic conversion, technologies and systems*, UIT Cambridge Ltd., Cambridge, England, 2016.
- ¹¹⁹S. Lany, *J. Chem. Phys.*, 2018, **148**, 071101.
- ¹²⁰A. Togo and I. Tanaka, *Scr. Mater.*, 2015, **108**, 1–5.

- ¹²¹A. P. Thompson, H. M. Aktulga, R. Berger, D. S. Bolintineanu, W. M. Brown, P. S. Crozier, P. J. in 't Veld, A. Kohlmeyer, S. G. Moore, T. D. Nguyen, R. Shan, M. J. Stevens, J. Tranchida, C. Trott and S. J. Plimpton, *Comp. Phys. Comm.*, 2022, **271**, 108171.
- ¹²²R. Freitas, M. Asta and M. de Koning, *Comput. Mater. Sci.*, 2016, **112**, 333–341.
- ¹²³F. C. Kracek, *J. Am. Chem. Soc.*, 1941, **63**, 1989–1990.
- ¹²⁴A. H. Larsen, J. J. Mortensen, J. Blomqvist, I. E. Castelli, R. Christensen, M. Dułak, J. Friis, M. N. Groves, B. Hammer, C. Hargus, E. D. Hermes, P. C. Jennings, P. B. Jensen, J. Kermode, J. R. Kitchin, E. L. Kolsbjerg, J. Kubal, K. Kaasbjerg, S. Lysgaard, J. B. Maronsson, T. Maxson, T. Olsen, L. Pastewka, A. Peterson, C. Rostgaard, J. Schiøtz, O. Schütt, M. Strange, K. S. Thygesen, T. Vegge, L. Vilhelmsen, M. Walter, Z. Zeng and K. W. Jacobsen, *J. Condens. Matter Phys.*, 2017, **29**, 273002.
- ¹²⁵J.-X. Shen and J. Varley, *J. Open Source Softw.*, 2024, **9**, 5941.
- ¹²⁶J.-X. Shen, L. F. Voss and J. B. Varley, *J. Appl. Phys.*, 2024, **135**, 145102.
- ¹²⁷S. P. Ong, W. D. Richards, A. Jain, G. Hautier, M. Kocher, S. Cholia, D. Gunter, V. L. Chevrier, K. A. Persson and G. Ceder, *Comput. Mater. Sci.*, 2013, **68**, 314–319.
- ¹²⁸A. Jain, S. P. Ong, G. Hautier, W. Chen, W. D. Richards, S. Dacek, S. Cholia, D. Gunter, D. Skinner, G. Ceder and K. A. Persson, *APL Materials*, 2013, **1**, 011002.
- ¹²⁹S. P. Ong, S. Cholia, A. Jain, M. Brafman, D. Gunter, G. Ceder and K. A. Persson, *Comput. Mater. Sci.*, 2015, **97**, 209–215.
- ¹³⁰L. Himanen, M. O. J. Jäger, E. V. Morooka, F. Federici Canova, Y. S. Ranawat, D. Z. Gao, P. Rinke and A. S. Foster, *Comput. Phys. Commun.*, 2020, **247**, 106949.
- ¹³¹J. Laakso, L. Himanen, H. Himm, E. V. Morooka, M. O. Jäger, M. Todorović and P. Rinke, *J. Chem. Phys.*, 2023, **158**, 234802.
- ¹³²L. McInnes, J. Healy, N. Saul and L. Großberger, *J. Open Source Softw.*, 2018, **3**, 861.
- ¹³³J. Qi, T. W. Ko, B. C. Wood, T. A. Pham and S. P. Ong, *Npj Comput. Mater.*, 2024, **10**, 43.
- ¹³⁴J. D. Hunter, *Comput. Sci. Eng.*, 2007, **9**, 90–95.
- ¹³⁵M. L. Waskom, *J. Open Source Softw.*, 2021, **6**, 3021.

- ¹³⁶A. Stukowski, *Model. Simul. Mater. Sci. Eng.*, 2010, **18**, 015012.
- ¹³⁷CrystalMaker®: a crystal and molecular structures program for Mac and Windows. CrystalMaker Software Ltd, Oxford, England (www.crystallmaker.com).
- ¹³⁸G. Henkelman, B. P. Uberuaga and H. Jónsson, *J. Chem. Phys.*, 2000, **113**, 9901–9904.
- ¹³⁹G. Henkelman and H. Jónsson, *J. Chem. Phys.*, 2000, **113**, 9978–9985.
- ¹⁴⁰F. Knoop, T. A. R. Purcell, M. Scheffler and C. Carbogno, *J. Open Source Softw.*, 2020, **5**, 2671.
- ¹⁴¹C. Chen, Y. Zuo, W. Ye, Q. Ji and S. P. Ong, *Maml - materials machine learning package*, <https://github.com/materialsvirtuallab/maml>, 2020.

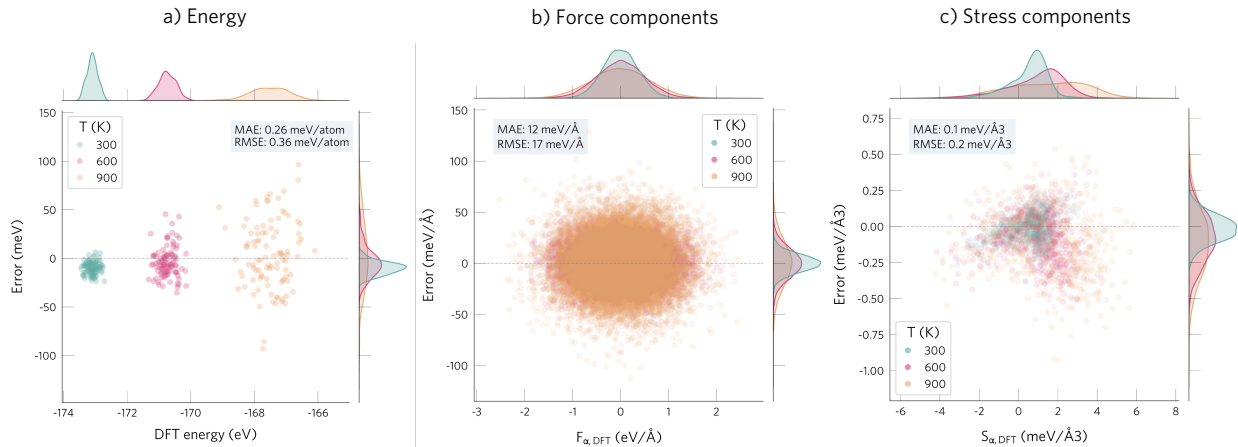
Supplementary Information for ‘Point defect formation at finite temperatures
with machine learning force fields’

1. MACHINE LEARNING FORCE FIELDS

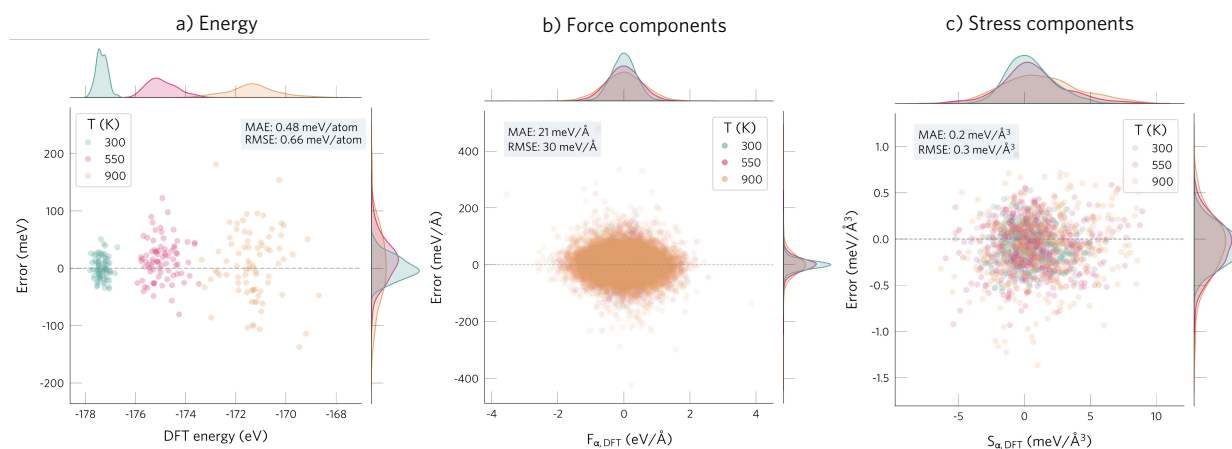
A. Validation on test set

Supplementary Table S1 Number of configurations in the datasets used to train and test each model. The training datasets are divided into training and validation sets (90% and 10%, respectively), with the latter used to monitor the validation loss during training. We note that we used more training configurations than necessary, as discussed in the 1 B.

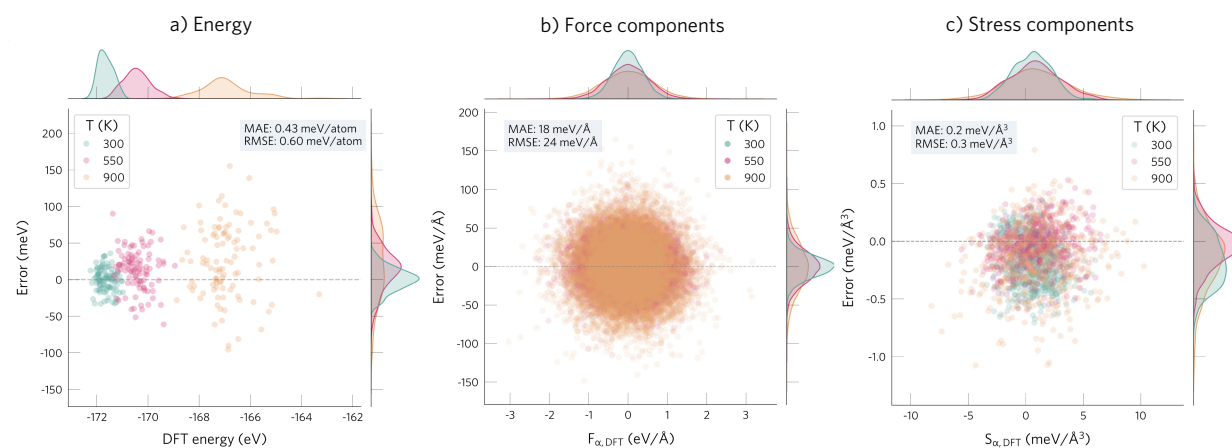
	CdTe	Te _i ⁺¹	V _{Te} ⁺²	Te
Train	1412	3992	4316	1171
Test	300	237	132	312



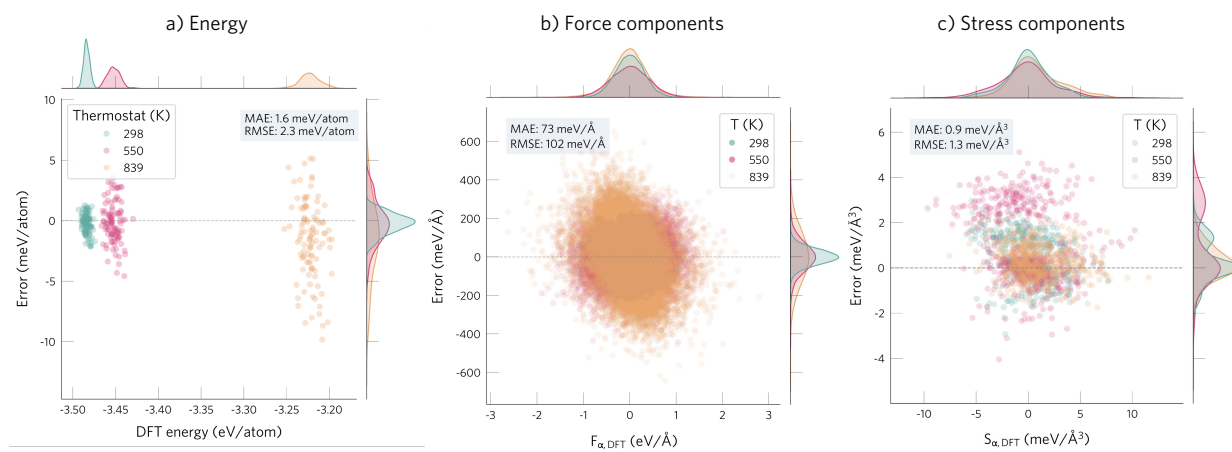
Supplementary Figure S1 Distribution of mean absolute and root mean squared errors (MAE, RMSE) for the test set of bulk CdTe.



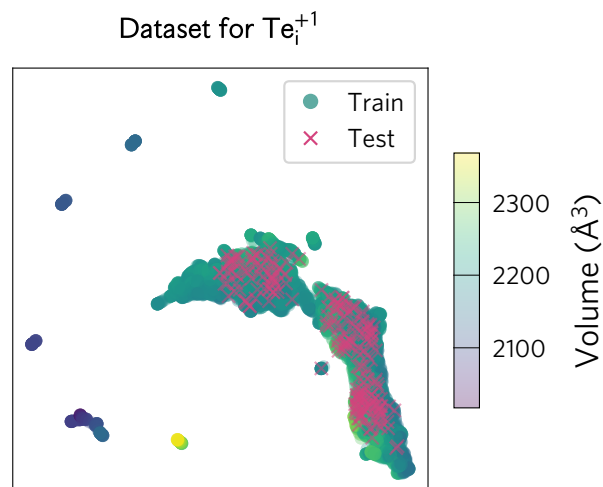
Supplementary Figure S2 Distribution of mean absolute and root mean squared errors (MAE, RMSE) for the test set of Te_i^{+1} . The distribution of the test and training configurations are illustrated in [Supplementary Figure S5](#).



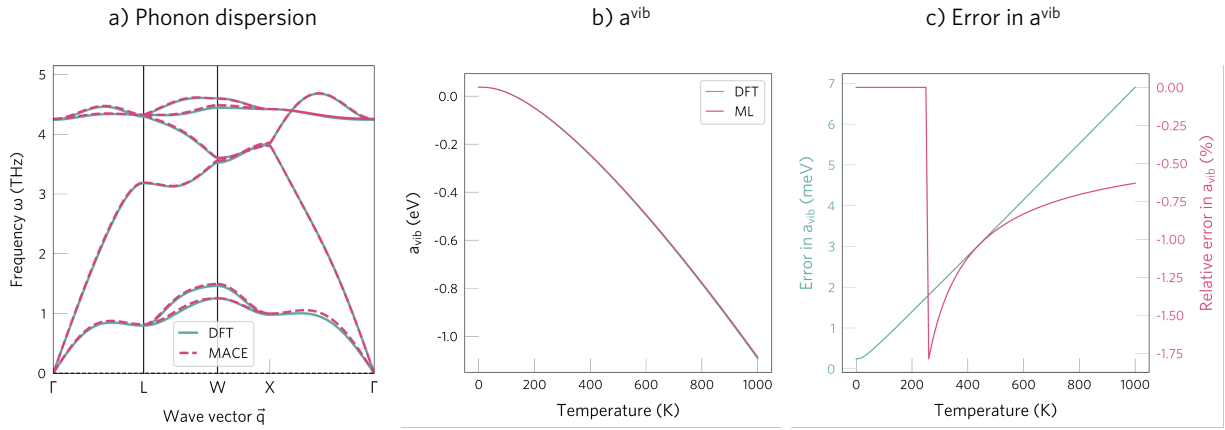
Supplementary Figure S3 Distribution of mean absolute and root mean squared errors (MAE, RMSE) for the test set of V_{Te}^{2+} .



Supplementary Figure S4 Distribution of mean absolute and root mean squared errors (MAE, RMSE) for the test set of Te. Note that Te melts at 720 K, leading to larger errors for the liquid phase ($T=900$ K).



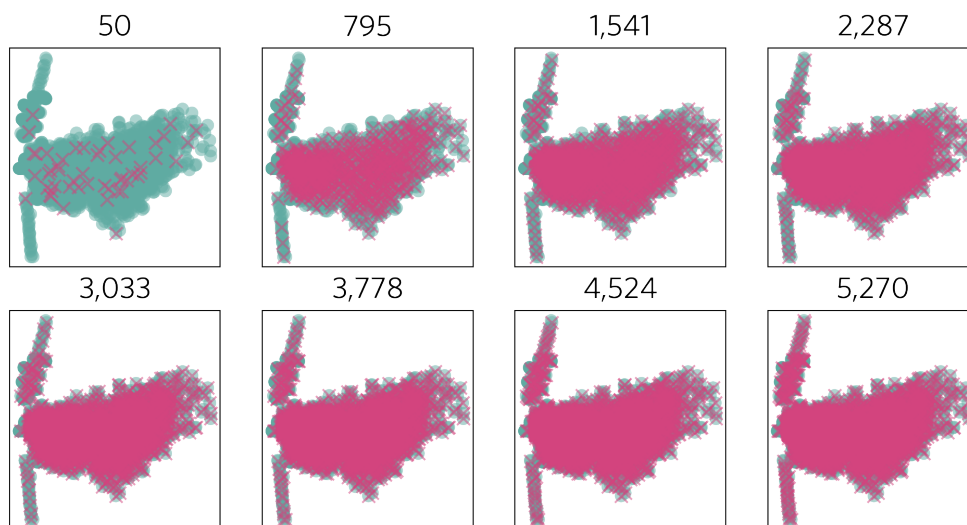
Supplementary Figure S5 Two-dimensional feature map for the configurations in the dataset of Te_i^{+1} . The configurations used for training are shown with circles, while the test ones are displayed with pink crosses. The isolated clusters of training datapoints correspond to compressed and expanded structures generated by scaling the equilibrium volume, which was necessary to ensure that the model could be applied with the quasiharmonic approximation. These regions were not included in the test set, which was designed to measure the accuracy of the model in typical application conditions (1 atm, 100-900 K), and accordingly expands over the configurations with equilibrium volumes at 1 atm. The good coverage of the test set over the training set feature space demonstrates its ability to quantify the accuracy of the model. Each configuration was encoded with its DIRECT descriptor (averaged over sites) and the dimensions were reduced using the Uniform Manifold Approximation, as implemented in the UMAP package¹³².



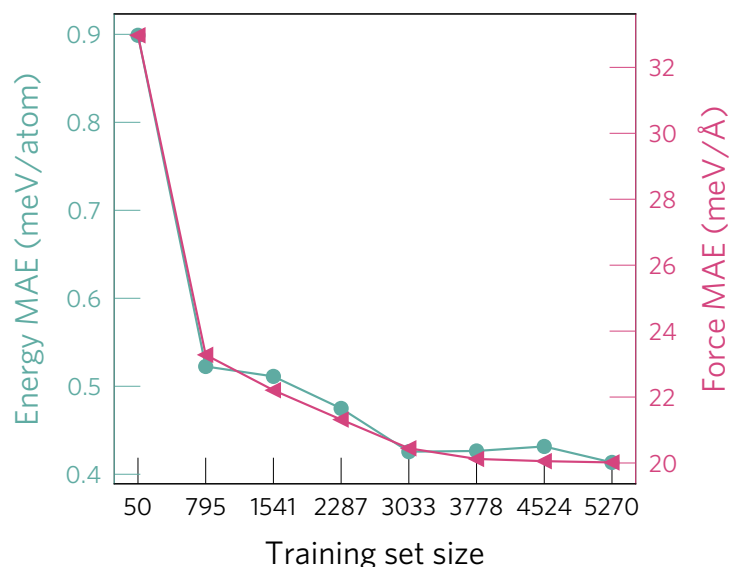
Supplementary Figure S6 Comparison of the harmonic phonon dispersion and vibrational free energy calculated with DFT and the DIRECT MLFF for bulk CdTe (primitive cell, 2 atoms). Note that the abrupt change in the relative error is caused by a^{vib} changing sign (i.e., division by 0 in $\Delta a = (a^{\text{ML}} - a^{\text{DFT}})/a^{\text{DFT}}$).

B. Learning curve

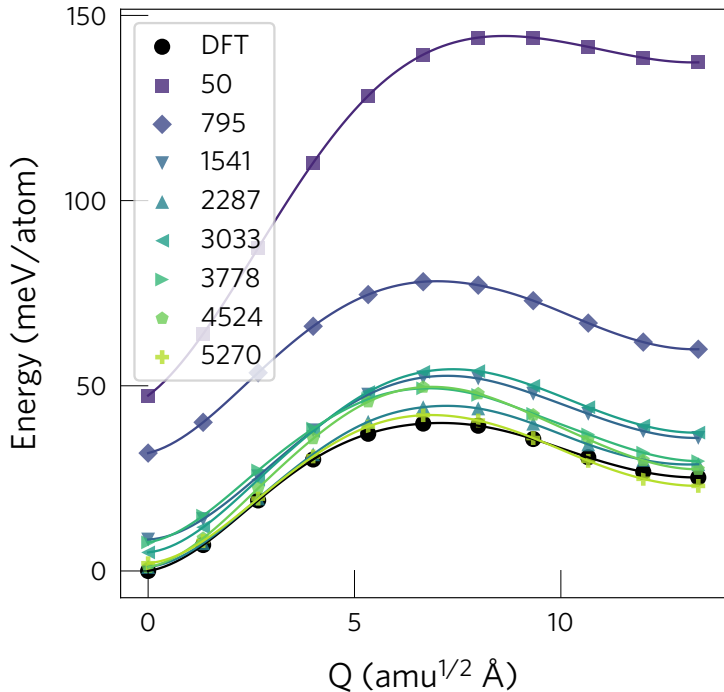
We analysed the learning curve for a model describing the behaviour of Te_i^{+1} at temperatures 100-900 K. We generated training sets with increasing number of configurations using the DIRECT method to sample the most diverse structures from the full dataset. This resulted in eight sets containing 50, 795, 1541, 2287, 3033, 3778, 4524 and 5270 configurations, which were used to train eight separate DIRECT models. By evaluating the performance of these models on the same test set (300 configurations, shown in [Supplementary Figure S5](#)), we can see that good accuracies ($\text{MAE}_E \leq 1 \text{ meV/atom}$) can be achieved with only 50 configurations ([Supplementary Figure S8](#)), as long as these are sampled to maximise their diversity. However, this accuracy level is not enough to properly capture the small energy differences between the stable configurations of Te_i^{+1} , which only differ by $\Delta E(C_{2v} - C_s)_{\text{DFT}} = 18 \text{ meV/supercell} = 0.3 \text{ meV/atom}$. As demonstrated in [Supplementary Figure S9](#), training sets with at least 1500 configurations are needed to accurately describe the barrier.



Supplementary Figure S7 Training sets of increasing size generated by sampling increasing number of configurations from the full dataset of 6016 Te_i^{+1} structures. Green circles illustrate the full dataset of configurations, while the selected structures are shown in pink crosses. Sampling was performed with the DIRECT algorithm¹³³. Each structure was encoded with its MACE descriptor (averaged over sites) and the dimensions were reduced using Principal Component Analysis, as implemented in the `maml` package¹⁴¹.



Supplementary Figure S8 Learning curve for the Te_i^{+1} machine learning force field, showing the energy and force mean absolute errors (MAE) on the test set for models with an increasing number of training configurations. The root mean square error shows a similar trend to the MAE. Models of acceptable accuracy ($\text{MAE}_E \leq 1$ meV/atom) can already be achieved with a small training set (50-1000 configurations), which is notable considering that the test set encompasses configurations from temperatures 300-900 K. The different training sets were generated by sampling the full dataset using the DIRECT algorithm¹³³ to ensure optimal coverage of the configurational landscape, as illustrated in [Supplementary Figure S7](#).



Supplementary Figure S9 Performance of the models with increasing training sizes on the energy barrier between the stable structures. Even for models with a low test error ($\text{MAE} < 0.5 \text{ meV/atom}$), the errors in the barrier are significant. This is caused by i) the small energy differences between the configurations

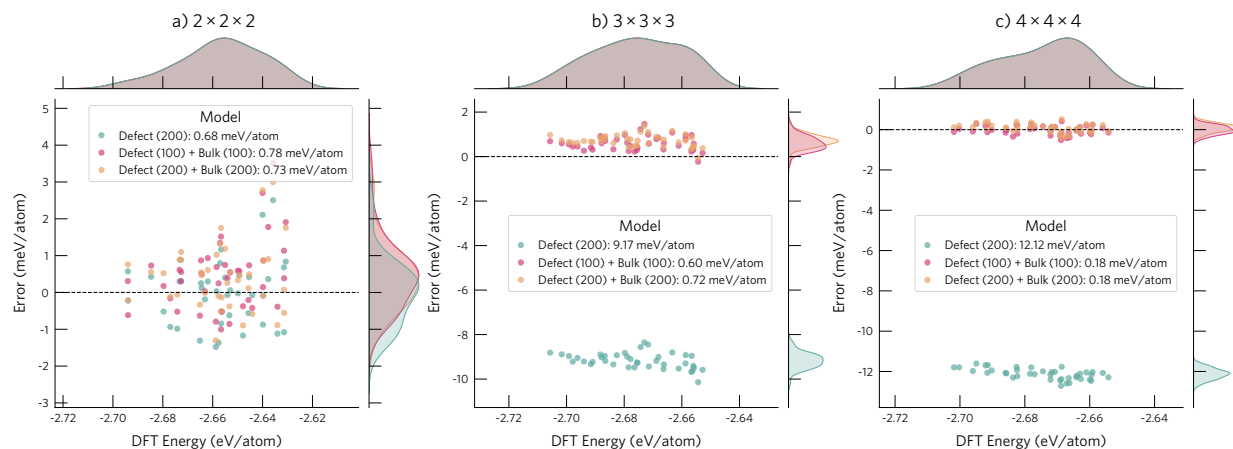
$$(E_{\text{barrier,DFT}} \approx 40 \text{ meV/supercell} = 0.6 \text{ meV/atom},$$

$\Delta E(C_{2v} - C_s)_{\text{DFT}} = 18 \text{ meV/supercell} = 0.3 \text{ meV/atom}$) and ii) the fact that the configurations in the training set are sampled to maximise diversity. This method samples most structures from the high energy region of the PES (and thus less structures from the 0 K path between the defect configurations). The legend denotes the number of configurations in the training set of each model, with the colormap ranging from dark purple to light green for increasing number of configurations. All energies are referenced to the DFT energy of the ground state configuration ($Q = 0 \text{ amu}^{1/2}\text{\AA}$).

C. Training machine learning force fields for defects

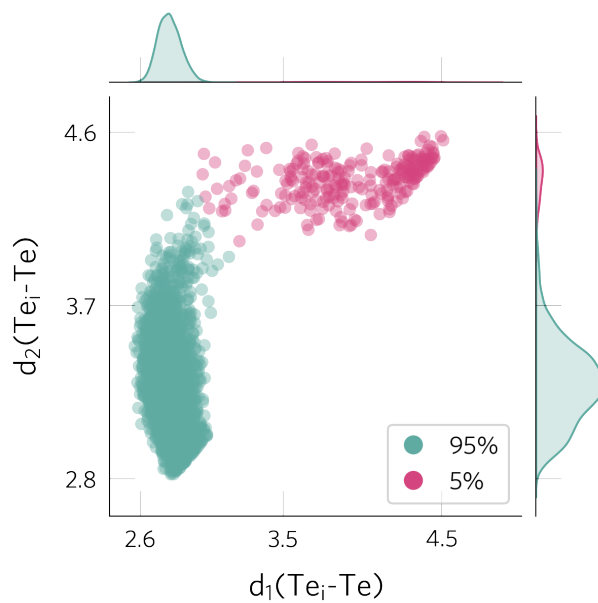
In this study, we trained separate MACE force fields for the pristine and defective supercells since this lead to higher accuracies. However, we have observed that this approach limits the defect models when applied to *larger supercells* than the ones used for training. While the models correctly describe the relative energies of the different configurations, they result in a systematic energy error. This is caused by how the MLFFs decompose the total energy into atomic contributions. When a model is trained only on *defect* configurations, part of the energy associated with the formation of the defect (e.g. one additional/missing atom and broken/reformed bonds) is spread over the energies of all atoms in the supercell. If the model is then applied to a larger supercell, the predicted atomic energies for bulk-like atoms do not correspond to the energy of an atom in a bulk-like environment, leading to a systematic energy shift ([Supplementary Figure S10.b](#)).

To solve this issue, one should train on *both* defect and pristine supercells. To illustrate this point, we trained three MACE models on three different datasets: i) 200 defect configurations of Te_i , ii) 100 defect (Te_i) and 100 pristine configurations and iii) 200 defect (Te_i) and 200 pristine configurations. Each dataset was sampled from the original training set ($2 \times 2 \times 2$ supercells) using the DIRECT method to maximise structural diversity. As illustrated in [Supplementary Figure S10](#), while the model trained only on defect configurations leads to a smaller MAE when validating on configurations with the same number of atoms as the training structures ($2 \times 2 \times 2$ supercell, 65 atoms), it results in a systematic error when applied to larger supercells ($3 \times 3 \times 3$ (217 atoms) and $4 \times 4 \times 4$ (513 atoms)). This leads to a general conclusion when training MLFFs for point or extended defects: the training dataset should include both defect and pristine configurations if the models will be applied to larger defect supercells.

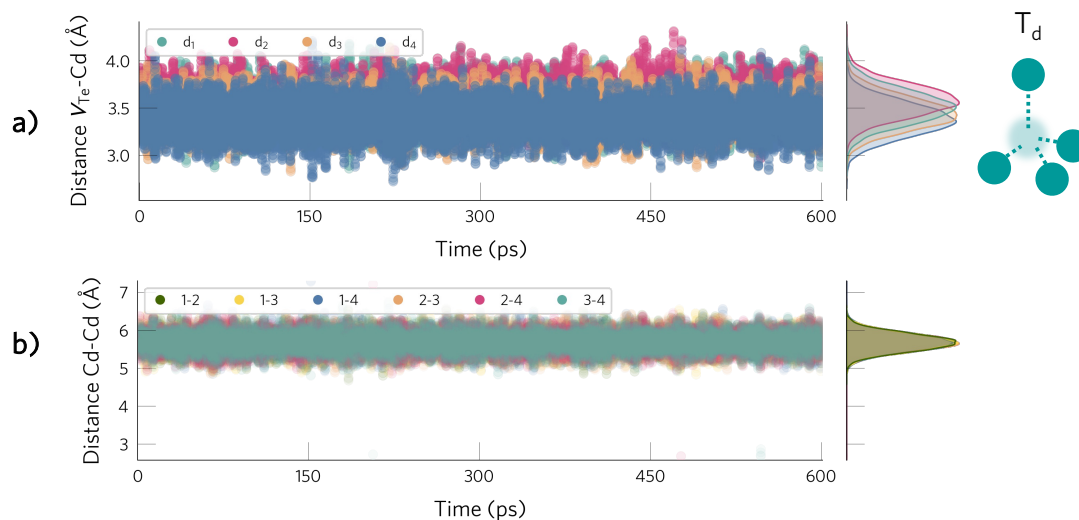


Supplementary Figure S10 Comparison of test errors between the energies predicted by the Te_i^0 models and DFT, when validated on supercells of different sizes: a) $2 \times 2 \times 2$, b) $3 \times 3 \times 3$ and c) $4 \times 4 \times 4$. Different colours correspond to the MACE models trained on different datasets: i) only defective structures of Te_i^0 (200 configurations), ii) 100 Te_i^0 structures and 100 pristine structures and iii) 200 Te_i^0 structures and 200 pristine structures. For each supercell size, the 40 test structures used for validation were sampled from heating runs (from 300 to 600 K with a heating rate of 0.7 K/ps) using the DIRECT method.

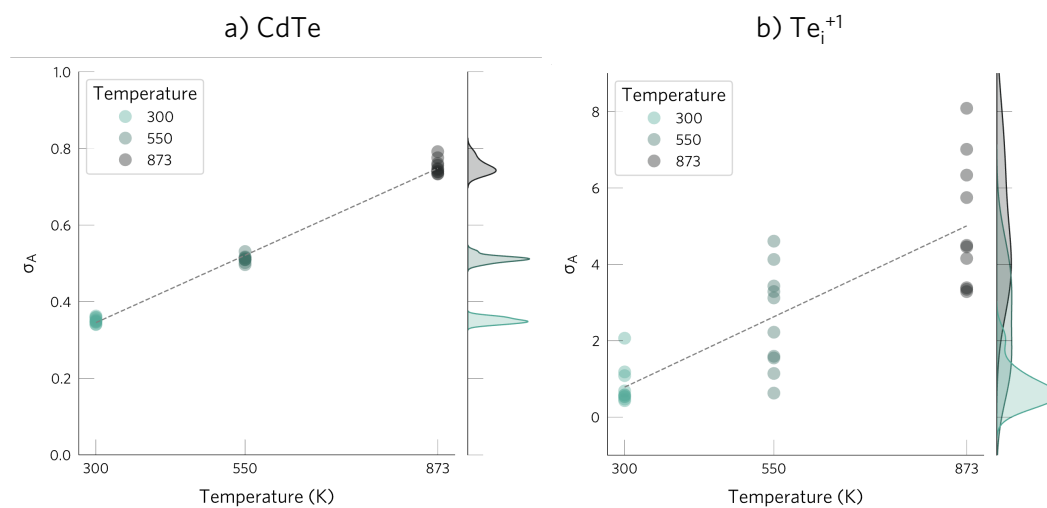
2. DYNAMIC ANALYSIS



Supplementary Figure S11 Changes in the configuration of Te_i^{+1} at 300 K, quantified by monitoring the shortest $\text{Te}_i\text{-Te}$ distances. While there is little variation in the shortest Te-Te bond (localised peak for d_1), the second shortest bond shows a wide variation ($d_2 = 2.8 - 4.0$ Å) — illustrating the change between the low-energy metastable configurations. Finally, there are some configurations where the interstitial occupies a significantly less favourable position without any Te-Te bonds (pink data points).

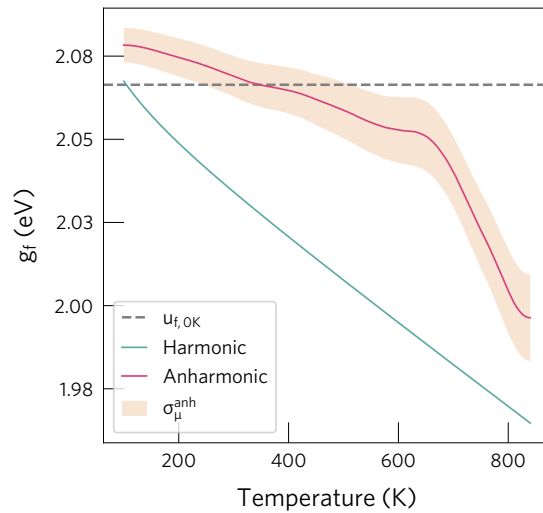


Supplementary Figure S12 Evolution of V_{Te}^{+2} at 1 atm and 300 K (NPT ensemble), which stays in its T_d configuration. a) Distance between the vacancy and its Cd neighbours, showing that all of them stay at a similar distance. b) Distance between the four Cd atoms neighbouring the vacancy, with these distances being similar and showing little variation with time.

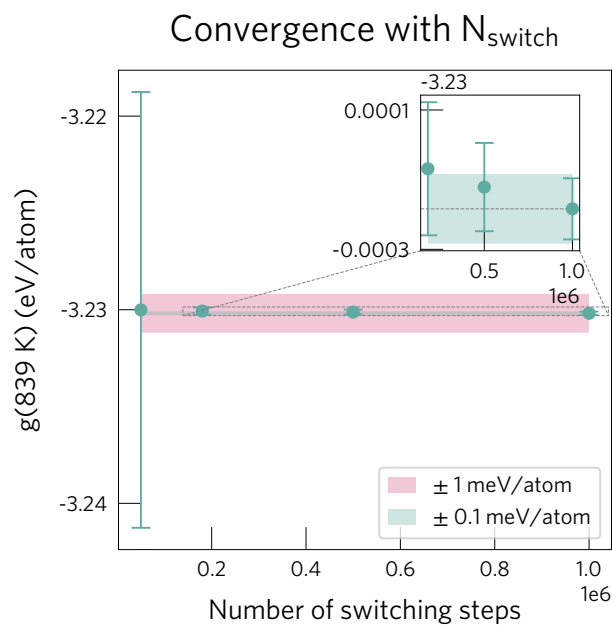


Supplementary Figure S13 Anharmonicity scores⁸⁷ for bulk CdTe and Te_i^{+1} , calculated on ten independent NPT trajectories (1 atm, $T=300, 550, 873$ K). The high anharmonicity scores of Te_i^{+1} are caused by its dynamic character (changes in configuration and position). For both bulk and the defect, the anharmonic character increases with temperature as the vibrational amplitude increases.

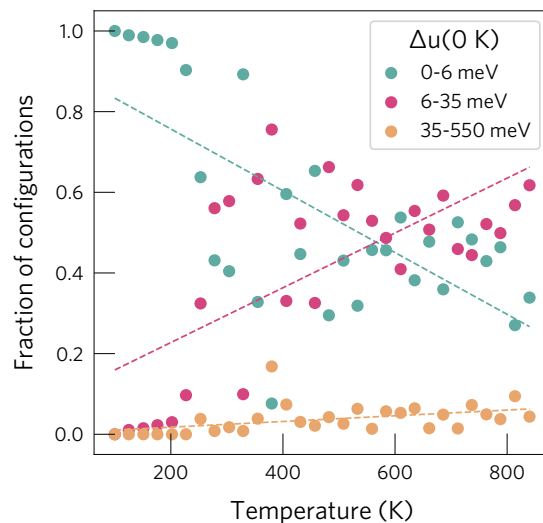
3. FREE ENERGIES



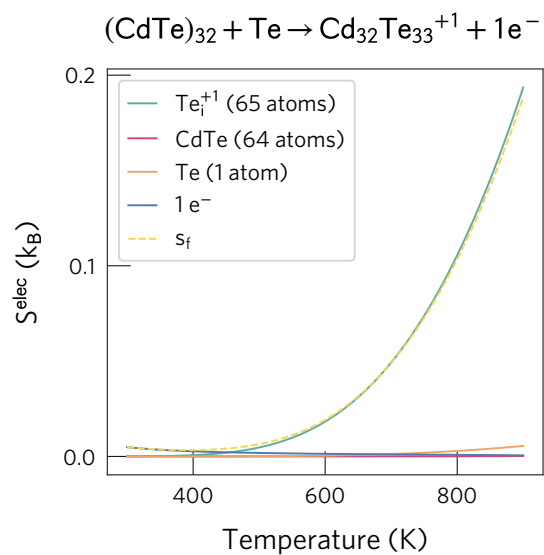
Supplementary Figure S14 Comparison of approximations for calculating the defect formation free energy, $g_f(T)$, of V_{Te}^{+2} . For comparison, the formation internal energy, $u_f(0 \text{ K})$, typically used in defect studies, is shown with a dashed grey line. This comparison shows that for V_{Te}^{+2} , entropic effects are negligible and barely affect $u_f(0 \text{ K})$ — which agrees with its static behaviour at room temperature (Supplementary Figure S12). Note that the change in slope of g_f^{anh} is caused by the change in the free energy of Te, which melts at 704 K.



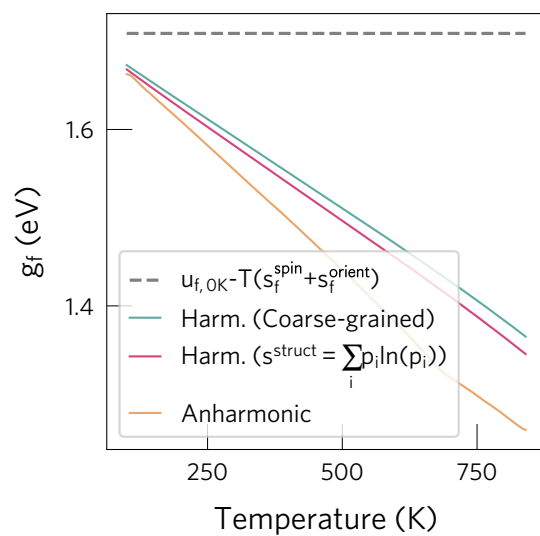
Supplementary Figure S15 Convergence of the temperature-dependent free energy of Te_i with respect to the number of switching steps used in the non-equilibrium thermodynamic integration simulations. The convergence is evaluated by comparing the values of the free energy at the end temperature (839 K). Note that differences below 0.1 meV/atom are achieved for $N_{\text{switch}} \geq 1.8 \times 10^5$ steps. The timestep was set to 2 fs and the uncertainties are determined by the mean standard error between 10 independent simulations performed for each value of N_{switch} .



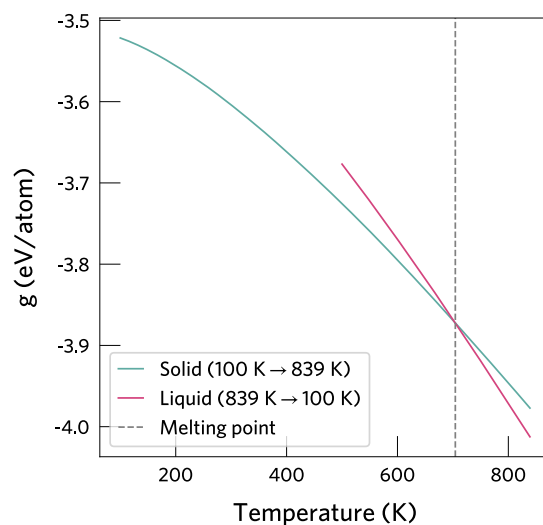
Supplementary Figure S16 Distribution of Te_i^{+1} in the ground state and metastable structures at different temperatures. The populations of the configurations are determined using the ‘Inherent structures’ formalism, by performing NPT MD simulations at different temperatures (80 ps, 1 atm), sampling 1600 equally-spaced configurations and relaxing them to their 0 K local minima using a conjugate gradient optimiser²⁵. While at low temperatures ($T > 200 \text{ K}$), the defect resides only in its lowest energy structure, above this temperature the population of the metastable configuration (i.e. the structure with higher internal energy) increases until it reaches the value of the ground state structure.



Supplementary Figure S17 Electronic entropy for the formation of Te_i^{+1} . The increase in entropy is caused by the defect introducing an empty electronic level 0.7 eV above the valence band maximum.



Supplementary Figure S18 Comparison of methods to calculate the structural or configurational entropy for the formation of Te_i^+ . The coarse-grained approach uses Equation (16) from the main text while the second method uses Equation (11), as explained in the Methods. Both approaches result in a similar formation free energy.



Supplementary Figure S19 Temperature variation of the Te free energy calculated with thermodynamic integration, showing the two independent integration paths and the resulting melting point (704 K), in reasonable agreement with the previously reported value of

722 K¹²³.